

AD-A182 165

METALLURGICAL CHARACTERIZATION OF ALUMINUM POWDER
CONSOLIDATION(U) MCDONNELL DOUGLAS RESEARCH LABS ST
LOUIS MO 5 N SASTRY ET AL MAY 87 MDC-01292

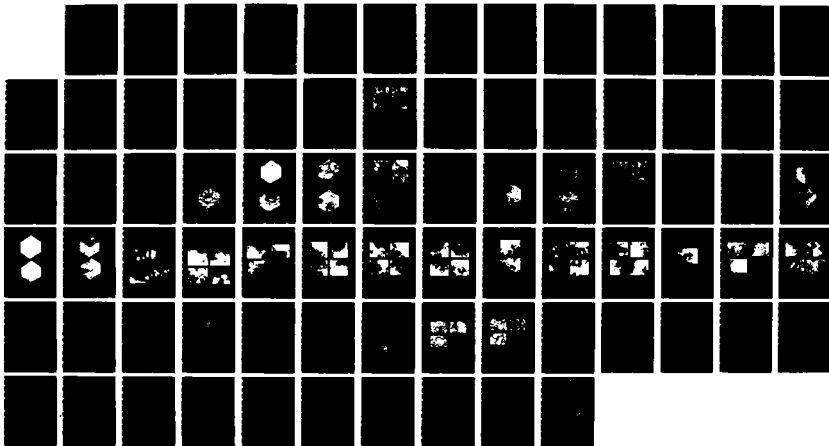
1/1

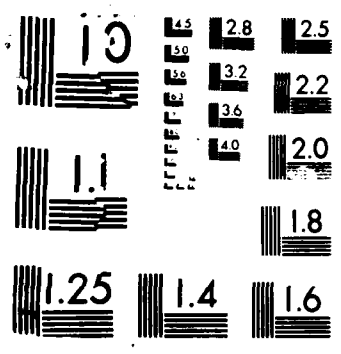
UNCLASSIFIED

AFOSR-TR-87-0814 F49620-83-C-0152

F/G 11/6

NL





DTIC FILE COPY

METALLURGICAL CHARACTERIZATION OF ALUMINUM POWDER CONSOLIDATION

AD-A182 165

S. M. L. Sastry
R. J. Lederich
T. C. Peng
J. E. O'Neal

McDonnell Douglas Research Laboratories
St. Louis, Missouri 63166

May 1987
Final Technical Report for the Period 1 September 1983 - 1 March 1987

Approved for public release; distribution unlimited

The views and conclusions contained in this document are those of the authors and should not be interpreted as necessarily representing the official policies or endorsements, either expressed or implied, of the Air Force Office of Scientific Research of the U.S. Government.

Prepared for:
UNITED STATES AIR FORCE
Air Force Office of Scientific Research
Bolling Air Force Base, DC 20332

McDonnell Douglas Research Laboratories

McDONNELL DOUGLAS

REPORT DOCUMENTATION PAGE		READ INSTRUCTIONS BEFORE COMPLETING FORM	
1. REPORT NUMBER AFOSR-TR- 87-0814	2. GOVT ACCESSION NO. AD-A182165	3. RECIPIENT'S CATALOG NUMBER	
4. TITLE (and Subtitle) METALLURGICAL CHARACTERIZATION OF ALUMINUM POWDER CONSOLIDATION		5. TYPE OF REPORT & PERIOD COVERED Final Technical Report 1 Sep. 1983-1 Mar. 1987	
7. AUTHOR(s) S. M. L. Sastry, R. J. Lederich, T. C. Peng, and J. E. O'Neal		6. PERFORMING ORG. REPORT NUMBER	
9. PERFORMING ORGANIZATION NAME AND ADDRESS McDonnell Douglas Research Laboratories McDonnell Douglas Corporation P.O. Box 516 St. Louis, MO 63166		8. CONTRACT OR GRANT NUMBER(s) F49620-83-C-0152	
11. CONTROLLING OFFICE NAME AND ADDRESS Air Force Office of Scientific Research Building 410 Bolling AFB, DC 20332		10. PROGRAM ELEMENT, PROJECT, TASK AREA & WORK UNIT NUMBERS 2306/A1	
14. MONITORING AGENCY NAME & ADDRESS (if different from Controlling Office) AFOSR/UE Bldg 410 Bolling AFB, DC 20332-6448		12. REPORT DATE May 1987	
16. DISTRIBUTION STATEMENT (of this Report) Approved for public release, distribution unlimited		13. NUMBER OF PAGES 78	
17. DISTRIBUTION STATEMENT (of the abstract entered in Block 20, if different from Report)		15. SECURITY CLASS. (of this report) Unclassified	
18. SUPPLEMENTARY NOTES		15a. DECLASSIFICATION/DOWNGRADING SCHEDULE	
19. KEY WORDS (Continue on reverse side if necessary and identify by block number) Aluminum alloys Powder metallurgy Rapid solidification Consolidation Hot pressing Extrusion Explosive consolidation Iron Densification Recovery Interparticle bonding Cerium Microstructure Porosity Lithium Zirconium Degassing Recrystallization			
20. ABSTRACT (Continue on reverse side if necessary and identify by block number) The influence of metallurgical and process variables on the consolidation, densification, and properties of rapidly solidified aluminum alloy powders was investigated. Cold compaction, hot pressing, powder extrusion, and explosive consolidation were used to consolidate rapidly solidified 99.9% aluminum powder (reference material), Al-3Li-1Cu-1Mg-0.2Zr (a representative low-density, high modulus alloy), and Al-8Fe-7Ce alloys (representative of high-temperature Al alloys). The alloys included in the study provide wide variations in hardness, flow stress, work hardening rate, plasticity, and oxide-fil thickness. The			

DD FORM 1 JAN 73 1473

EDITION OF 1 NOV 65 IS OBSOLETE

Unclassified

SECURITY CLASSIFICATION OF THIS PAGE (When Data Entered)

consolidation techniques selected for the study provide variations in pressure, compaction rate, and extent of oxide-film breakdown.

Three 35-kg lots of rapidly solidified 99.9% Al, Al-3Li-1Cu-1Mg-0.2Zr, and Al-8Fe-7Ce alloy powders were prepared by vacuum atomization, and the powders were characterized with respect to particle size distribution, cooling rates, constituent phases, and volatile contaminants.

The pressure dependence of densification during cold compaction was correlated with the yield stress and work hardening of the three alloys. Complete densification with sound interparticle bonding was observed in 99.9% Al powders hot pressed at 400°C. The hot-pressed Al-Li and Al-Fe-Ce alloys contained 1-2% porosity and had weak interparticle bonding. The extrusion rate dependences of flow stress and interparticle bonding were determined for 99.9% Al and Al-Li alloy powder compacts. The rate sensitivity of flow stress for Al and Al-Li alloys was ≈ 0.2 at extrusion rates of 0.04-0.6 cm/s. Extrusions of Al at > 0.04 cm/s resulted in fully densified compacts with sound interparticle bonding and recrystallized elongated grain microstructure. The Al-Li alloy extruded at > 0.08 cm/s showed sound interparticle bonding and recovered subgrain microstructure.

In aluminum, the dislocation cell size increases with increasing extrusion temperature and decreasing strain rate. Al-Li alloys develop a fine (0.5-1.0 μm diameter) dislocation substructure; the cell size is independent of extrusion temperature and strain rate. Extrusion of Al-Li alloys at 400°C, strain rate of 0.86 s^{-1} , and reduction ratio of 16:1 produces best combination of ultimate tensile strength of 559 MPa, ductility of 5.4%, and fracture toughness of 36.6 MPa. Al-Fe-Ce alloys extruded at $\leq 430^\circ\text{C}$ have fine dispersoids for high temperature creep resistance. Fully dense crack-free compacts with sound interparticle bonding were produced by explosive consolidation using fly tube. Tensile strengths of the explosively consolidated compacts were 72-98% of the strengths of extruded samples.

Unclassified

PREFACE

This report was prepared by the McDonnell Douglas Research Laboratories (MDRL), St. Louis, MO, for the Air Force Office of Scientific Research (AFOSR), Bolling AFB, DC, under Contract F49620-83-C-0152. The AFOSR Program Manager was Dr. A. H. Rosenstein.

The work was performed in the Solid State Sciences Department of MDRL under the supervision of Dr. C. R. Whitsett. The principal investigator was Dr. S. M. L. Sastry; co-investigators were Dr. T. C. Peng, Mr. R. J. Lederich, and Mr. J. E. O'Neal.

This report has been reviewed and is approved.



C. R. Whitsett
Director - Research
McDonnell Douglas Research Laboratories



D. P. Ames
General Manager - MDC Distinguished Fellow
McDonnell Douglas Research Laboratories



Accession For	
NTIS CRA&I	<input checked="" type="checkbox"/>
DTIC TAB	<input type="checkbox"/>
Unannounced	<input type="checkbox"/>
Justification	
By	
Distribution	
Availability Codes	
Dist	Avail and/or Special
A-1	

TABLE OF CONTENTS

Section	Page
1. INTRODUCTION.....	1
2. RESEARCH OBJECTIVES AND APPROACH.....	3
3. PREPARATION, CHARACTERIZATION, AND COLD COMPACTION OF RAPIDLY SOLIDIFIED ALUMINUM ALLOYS.....	5
3.1 Alloy Preparation.....	5
3.2 Powder Characterization.....	5
3.3 Consolidation of Aluminum Alloys Powders.....	15
3.3.1 Cold Compaction.....	15
4. HIGH TEMPERATURE CONSOLIDATION AND EXPLOSIVE CONSOLIDATION OF RAPIDLY SOLIDIFIED ALUMINUM ALLOYS.....	24
4.1 Vacuum Outgassing.....	24
4.2 Hot Pressing.....	24
4.3 Isothermal Powder Extrusion.....	27
4.4 Production Size Extrusions.....	45
4.5 Explosive Compaction of Aluminum Alloys.....	45
5. CONSOLIDATION PROCESS, MICROSTRUCTURE, AND PROPERTY INTER- RELATIONSHIP IN RAPIDLY SOLIDIFIED ALUMINUM ALLOYS.....	54
5.1 Flow Stress - Strain Rate Relationships.....	54
5.2 Consolidation Process Modeling.....	54
5.3 Interrelationship Between Consolidation Process and Product Mechanical Properties.....	57
5.3.1 Properties of Isothermal Extrusions.....	57
5.3.2 Properties of Production Size Extrusions.....	57
5.3.3 Properties of Explosively Consolidated Compacts.....	58
6. PUBLICATIONS AND PRESENTATIONS RESULTING FROM AFOSR SUPPORT.....	64
7. LIST OF PERSONNEL.....	65
8. COUPLING ACTIVITIES WITH GROUPS DOING RELATED RESEARCH.....	66
9. REFERENCES.....	67

LIST OF ILLUSTRATIONS

Figure	Page
1. Vacuum atomization apparatus.....	6
2. Particle size distributions of aluminum, Al-3Li-1Cu-1Mg-0.2Zr, and Al-8Fe-7Ce powders.....	7
3. Scanning electron micrographs of rapidly solidified (a) 99.9% Al, (b) Al-3Li-1Cu-1Mg-0.2Zr, (c) Al-8Fe-7Ce, and (d) Al-8Fe-4Ce powders.....	8
4. X-ray diffraction peaks of (a) aluminum, (b, c, and d) Al-3Li-1Cu-1Mg-0.2Zr alloy, (b) rapidly solidified, (c) annealed at 400°C for 2 h, and (d) annealed at 500°C for 2 h.....	10
5. X-ray diffraction peaks of (a) aluminum, (b, c, and d) Al-8Fe-4Ce alloy, (b) rapidly solidified, (c) annealed at 400°C for 2 h, and (d) annealed at 500°C for 2 h.....	11
6. X-ray diffraction peaks of (a) aluminum, (b, c, and d) Al-8Fe-7Ce alloy, (b) rapidly solidified, (c) annealed at 400°C for 2 h, and (d) annealed at 500°C for 2 h.....	12
7. Ion intensity as a function of temperature for aluminum Al-3Li-1Cu-1Mg-0.2Zr, Al-8Fe-7Ce, and Al-8Fe-4Ce alloy powders. (Data obtained by mass spectroscopic analysis.).....	14
8. Variation with compaction pressure of (a) density and (b) rate of density change with pressure (dp/dP) for aluminum, Al-3Li-1Cu-1Mg-0.2Zr, Al-8Fe-4Ce, and Al-8Fe-7Ce powders consolidated by uniaxial pressing at 25°C.....	16
9. Effect of powder-size distribution on (a) densification and (b) rate of density change with pressure (dp/dP) of aluminum powders consolidated by uniaxial pressing at 25°C. Powder size ranges: 10-260 μm, < 38 μm, and 125-180 μm.....	17
10. Effect of ram-displacement rate on densification of aluminum-powder compacts consolidated by uniaxial pressing at 25°C. Initial powder compact height is 1.75 cm, final powder compact height is 0.75 cm. Ram displacement rates: 2.5×10^{-3} cm/s, 5.0×10^{-3} cm/s, and 1.0×10^{-2} cm/s.....	18
11. Variation of density with compaction pressure for (a) aluminum and (b) Al-3Li-1Cu-1Mg-0.2Zr alloy powders consolidated by uniaxial pressing at 25°C: experimental values and calculated from Equation (4).....	19

LIST OF ILLUSTRATIONS
(continued)

Figure	Page
12. Variation of (a) density with effective stress and (b) density with the ratio of effective stress to yield stress of aluminum and Al-3Li-1Cu-1Mg-0.2Zr.....	20
13. Scanning electron micrographs of aluminum-powder compacts consolidated by uniaxial pressing at 25°C.....	20
14. Scanning electron micrographs of aluminum-powder compacts (with < 38- μ m-diam powders) consolidated by uniaxial pressing at 25°C..	21
15. Scanning electron micrographs of aluminum-powder compacts (with 125 to 180- μ m-diam powders) consolidated by uniaxial pressing at 25°C.....	21
16. Scanning electron micrographs of Al-3Li-1Cu-1Mg-0.2Zr alloy powder compacts consolidated by uniaxial pressing at 25°C.....	22
17. Scanning electron micrographs of Al-8Fe-7Ce alloy powder compacts consolidated by uniaxial pressing at 25°C.....	22
18. High-magnification electron micrographs of (a) aluminum, (b) Al-3Li-1Cu-1Mg-0.2Zr, and (c) Al-8Fe-7Ce alloy powder compacts consolidated by uniaxial pressing at 25°C.....	23
19. Optical micrographs of aluminum powder compacts consolidated by uniaxial pressing at 400°C.....	25
20. Optical micrographs of Al-3Li-1Cu-1Mg-0.2Zr alloy powder compacts consolidated by uniaxial pressing at 400°C.....	26
21. Optical micrographs of Al-8Fe-7Ce alloy powder compacts consolidated by uniaxial pressing at 400°C.....	26
22. High-magnification scanning electron micrographs of (a) Al-3Li-1Cu-1Mg-0.2Zr and (b) Al-8Fe-7Ce alloy powder compacts consolidated by uniaxial pressing at 400°C.....	27
23. Variation of flow stress with extrusion rate of (o) aluminum and (Δ) Al-3Li-1Cu-1Mg-0.2Zr powders extruded at 400°C.....	29
24. Optical micrographs of aluminum powder compacts extruded at 400°C at extrusion rates of (a) 0.01 cm/s, (b) 0.04 cm/s, (c) 0.08 cm/s, and (d) 0.16 cm/s.....	30
25. Optical micrographs of Al-3Li-1Cu-1Mg-0.2Zr alloy powder compacts extruded at 400°C at extrusion rates of (a) 0.02 cm/s and (b) 0.08 cm/s.....	32

LIST OF ILLUSTRATIONS
(continued)

Figure	Page
26. Transmission electron micrographs of 99.99% Al powders extruded at 350°C with an area reduction of 16:1. (a,b) vacuum outgassed at 500°C, (c,d) without vacuum outgassing; (a,c) strain rate of 1.59/s, (b,d) strain rate of 0.23/s.....	33
27. Transmission electron micrographs of 99.99% Al powders extruded at 400°C with an area reduction ratio of 16:1. (a,b) vacuum outgassed at 500°C, (c,d) without vacuum outgassing; (a,c) strain rate of 1.59/s, (b,d) strain rate of 0.23/s.....	34
28. Transmission electron micrographs of 99.99% Al powders extruded at 450°C with an area reduction of 16:1. (a,b) without vacuum outgassing, (c) vacuum outgassed at 500°C; (a,c) strain rate of 1.59/s, (b) strain rate of 0.23/s.....	35
29. Transmission electron micrographs of Al-3Li-1Cu-1Mg-0.2Zr alloy powders vacuum outgassed at 500°C and extruded at 350°C with an area reduction ratio of 16:1. (a,b) strain rate of 1.59/s, (c,d) strain rate of 0.23/s; (a,c) longitudinal section, (b,d) transverse section.....	36
30. Transmission electron micrographs of Al-3Li-1Cu-1Mg-0.2Zr alloy powders vacuum outgassed at 500°C and extruded at 400°C with an area reduction ratio of 16:1. (a,b) strain rate of 1.59/s, (c,d) strain rate of 0.23/s; (a,c) longitudinal section, (b,d) transverse section.....	37
31. Transmission electron micrographs of Al-3Li-1Cu-1Mg-0.2Zr alloy powders extruded at 350°C (without vacuum outgassing) with an area reduction ratio of 16:1. (a,b) strain rate of 1.59/s, (c,d) strain rate of 0.23/s; (a,c) longitudinal section, (b,d) transverse section.....	38
32. Transmission electron micrographs of Al-3Li-1Cu-1Mg-0.2Zr alloy powders extruded at 400°C (without vacuum outgassing) with an area reduction ratio of 9:1 and strain rate of 1.59/s, (a) longitudinal section and (b) transverse section.....	39
33. Transmission electron micrographs of Al-3Li-1Cu-1Mg-0.2Zr alloy vacuum outgassed at 500°C and extruded at 430°C with an area reduction ratio of 16:1. (a,b) strain rate of 1.59/s, (c,d) strain rate of 0.23/s; (a,c) longitudinal section, (b,d) transverse section.....	40
34. Transmission electron micrographs of Al-3Li-1Cu-1Mg-0.2Zr alloy powders extruded at 400°C (without vacuum outgassing) with an area reduction ratio of 16:1. (a,b) strain rate of 1.59/s, (c,d) strain rate of 0.23/s; (a,c) longitudinal section, (b,d) transverse section.....	41

LIST OF ILLUSTRATIONS
(continued)

Figure	Page
35. Transmission electron micrographs of Al-3Li-1Cu-1Mg-0.2Zr alloy powders extruded at 430°C (without vacuum outgassing) with an area reduction ratio of 16:1 and strain rate of 1.59/s, (a,c) longitudinal section.....	42
36. Transmission electron micrographs of Al-8Fe-4Ce alloy powders; (a) as rapidly solidified, (b) annealed at 400°C for 2 h, and (c) annealed at 500°C for 2 h.....	43
37. Transmission electron micrographs of Al-8Fe-7Ce alloy powders; (a,b) as rapidly solidified, (c) annealed at 400°C for 2 h, and (d) annealed at 500°C for 2 h.....	44
38. High-energy consolidation of rapid solidification processed (RSP) alloys.....	46
39. Powder pack as assembled.....	47
40. Test arrangement for explosive compaction with detonation velocity measurement.....	48
41. Pressure profiles and wave patterns during explosive compactions.	50
42. Optical micrographs of explosive compacts of (a) 99.9% Al, (b) Al-3Li-1Cu-1Mg-0.2Zr, and (c) Al-8.4Fe-7Ce alloys.....	51
43. Scanning electron micrographs of tensile fracture of explosive consolidated (a) 99.9% Al, (b) Al-3Li-1Cu-1Mg-0.2Zr, and (c) Al-8.4Fe-7Ce alloys.....	52
44. Scanning electron micrographs of tensile fractures of explosively consolidated (a) 99.9% Al, (b) Al-3Li-1Cu-1Mg-0.2Zr, and (c) Al-8Fe-7Ce alloys.....	53
45. Effect of extrusion temperature and strain rate on extrusion flow stress for unalloyed Al.....	55
46. Effect of isothermal extrusion temperature and strain rate on co-content J of unalloyed aluminum.....	55
47. Effect of extrusion temperature and strain rate on extrusion flow stress for Al-3Li-1Cu-1Mg-0.2Zr.....	56
48. Effect of isothermal extrusion temperature and strain rate on co-content J of Al-3Li-1Cu-1Mg-0.2Zr.....	56
49. Effect of extrusion ratio (R) and strain rate on the room temperature yield stress of unalloyed aluminum isothermally extruded at 400°C.....	57

LIST OF ILLUSTRATIONS
(continued)

Figure	Page
50. Effect of extrusion temperature and strain rate on the room temperature yield stress of unalloyed aluminum isothermally extruded at a ratio of 16:1.....	58
51. Effect of extrusion R ratio and strain rate on room temperature yield stress of Al-3Li-1Cu-1Mg-0.2Zr isothermally extruded at 400°C.....	62
52. Effect of extrusion temperature and strain rate on room-temperature yield stress of Al-3Li-1Cu-1Mg-0.2Zr isothermally extruded at a ratio of 16:1.....	63

LIST OF TABLES

Table	Page
1. Nominal compositions and chemical analyses of the materials studied.....	6
2. Indentation dimensions and microhardness values of powders studied.....	9
3. Interplanar spacing (d) of phases detected in Al-8Fe-7Ce alloy annealed at 500°C for 2 h.....	13
4. Tap densities and theoretical densities of materials studied...	15
5. Bulk hydrogen and oxygen concentrations of P/M aluminum alloys before and after vacuum outgassing.....	24
6. Test parameters and consolidate properties for explosive compactions (3590 m/s measured detonation speed and 3.7 GPa estimated peak pressure).....	49
7. Effects of extrusion parameters on mechanical properties of unalloyed aluminum in as-extruded condition.....	59
8. Effect of extrusion parameters on mechanical properties of Al-3Li-1Cu-1Mg-0.2Zr after solution treatment and aging (560°C/1 h/WQ; 177°C/24 h/AC).....	60
9. Effect of extrusion parameters on mechanical properties of Al-8Fe-7Ce in as-extruded condition.....	61
10. Effect of extrusion parameters on mechanical properties of Al-8Fe-7Ce in as-extruded condition.....	62

1. INTRODUCTION

Rapid solidification processing (RSP) through its ability to refine microstructures and increase solid solubilities has made the development of new aluminum alloys systems possible.¹⁻⁵ These alloy systems include the low-density, high-modulus, precipitation-hardenable Al-Li alloys,^{1,2} high-temperature dispersion-strengthened Al-Fe-Ce alloys,³ high-strength Al-Zn-Mg alloys,⁴ and SiC whisker-reinforced aluminum alloys.⁵

The overall RSP sequence involves the rapid solidification of alloys into powder by atomization or into flakes by splat quenching followed by consolidation of the particulates into fully dense alloys. Consolidation steps include cold compaction of the particulates to about 70% of the theoretical density, vacuum hot pressing to fully densify the cold compacts, and extrusion or forging. The most important consideration for realizing the full benefits of rapidly solidified aluminum powders is optimization of the powder consolidation parameters. The powder size and shape, temperature, strain, strain rate, and type of deformation during consolidation determine the extent of densification, substructure formation, recovery and recrystallization, second-phase precipitation or resolution, and texture development. These metallurgical changes determine the microstructures and properties that can be achieved by post-consolidation thermomechanical processing and heat treatment. The most important consolidation-related microstructural features that deleteriously affect the mechanical properties of a consolidate are: (1) particle delamination as a result of improper breakdown of oxide film and poor interparticle bonding, (2) hydrogen blistering resulting from improper degassing or moisture pickup during powder preparation and consolidation, and (3) directionality in properties resulting from crystallographic texture development during consolidation. Each of these features is influenced by the method of powder consolidation.

Despite the overwhelming importance of aluminum powder compaction, especially in the case of rapidly solidified aluminum alloy powders, no systematic study has been made of the interrelationship between powder and process variables and the resultant microstructures and mechanical properties of compacts. We report here the results of a systematic study of the influence of selected metallurgical and process variables on the consolidation, densification, and properties of rapidly solidified aluminum alloy powders. Aluminum (99.9% pure

reference material), a representative low-density high-modulous Al-Li alloy, and a representative high-temperature dispersion-strengthened Al-Fe-Ce alloy were selected to determine the effects of metallurgical parameters on consolidation. The selected alloys have wide variations in hardness, flow stress, work hardening rate, plasticity, and oxide-film thickness. Vacuum hot pressing, hot isostatic pressing, powder extrusion, and explosive compaction have been selected for evaluating consolidation process parameters. The consolidation techniques selected for the study provide variations in pressure, compaction rate, and extent of oxide-film breakdown.

The goal of the program was to construct consolidation diagrams in a manner analogous to superplastic forming and sintering diagrams. Such generalized relations and consolidation diagrams can be used to optimize consolidation variables, obtain beneficial combinations of properties in products processed from rapidly solidified powders, and provide guidelines for consolidation and near-net-shape processing of aluminum alloy powders.

2. RESEARCH OBJECTIVES AND APPROACH

The overall objectives of this program were to (1) determine the effects of powder shape, size, size distribution, surface-oxide film, entrapped hydrogen, and powder plastic-flow characteristics on densification, interparticle bonding, and microstructure development during consolidation by hot pressing, extrusion, and dynamic compaction; (2) determine the effects of consolidation process variables (temperature, pressure, and compaction rate) on the microstructures and mechanical properties of aluminum alloy powder compacts; and (3) establish generalized relations between material and process variables and construct consolidation diagrams to provide guidelines for selecting and optimizing aluminum alloy consolidation schedules.

The research described in this report was conducted in three phases.

Phase I: Preparation, Characterization, and Cold Compaction of Rapidly Solidified Aluminum Alloys

Three 35-kg lots of rapidly solidified 99.9% Al, Al-3Li-1Cu-1Mg-0.2Zr, and Al-8Fe-7Ce alloy powders were prepared by vacuum atomization; and the powders were characterized with respect to particle size distribution, cooling rates, constituent phases, and volatile contaminants. Tap densities and cold compacted densities of the powders were determined. The effects of powder parameters on the densification during cold compaction were determined and the pressure dependences of densification during cold compaction were correlated with the yield stress and work hardening of the three alloys.

Phase II: Slow-, Medium-, and High-Strain Rate Consolidation of Rapidly Solidified Aluminum Powders

Rapidly solidified aluminum alloy powders were consolidated by cold compaction to 60-70% density followed by extrusion at 300-500°C with extrusion ratios of 9:1, 16:1 and 36:1 and aspect ratios of 1:1 to 5:1, and explosive compaction (high strain rate compaction) at 25°C and pressures of 0.1-1.0 GPa. Powder densification, interparticle bonding, oxide break-up and distribution, and recovery and recrystallization were determined in the consolidated products. The dependences of percent densification and densification rate on material and process variables were determined.

Phase III: Consolidation Process, Microstructure, and Property Optimization of Rapidly Solidified Aluminum Alloys

Consolidation diagrams showing the interrelations between material and process variables were constructed. The microstructures and tensile properties at 25°C of powders compacted by extrusion and explosive consolidation were determined. Generalized relations between powder and process variables, and microstructures and tensile properties of consolidated rapidly solidified aluminum products were established. The effectiveness of various consolidation techniques was assessed and guidelines for process and property optimization were formulated.

3. PREPARATION, CHARACTERIZATION, AND COLD COMPACTION OF RAPIDLY SOLIDIFIED ALUMINUM ALLOYS

3.1 Alloy Preparation

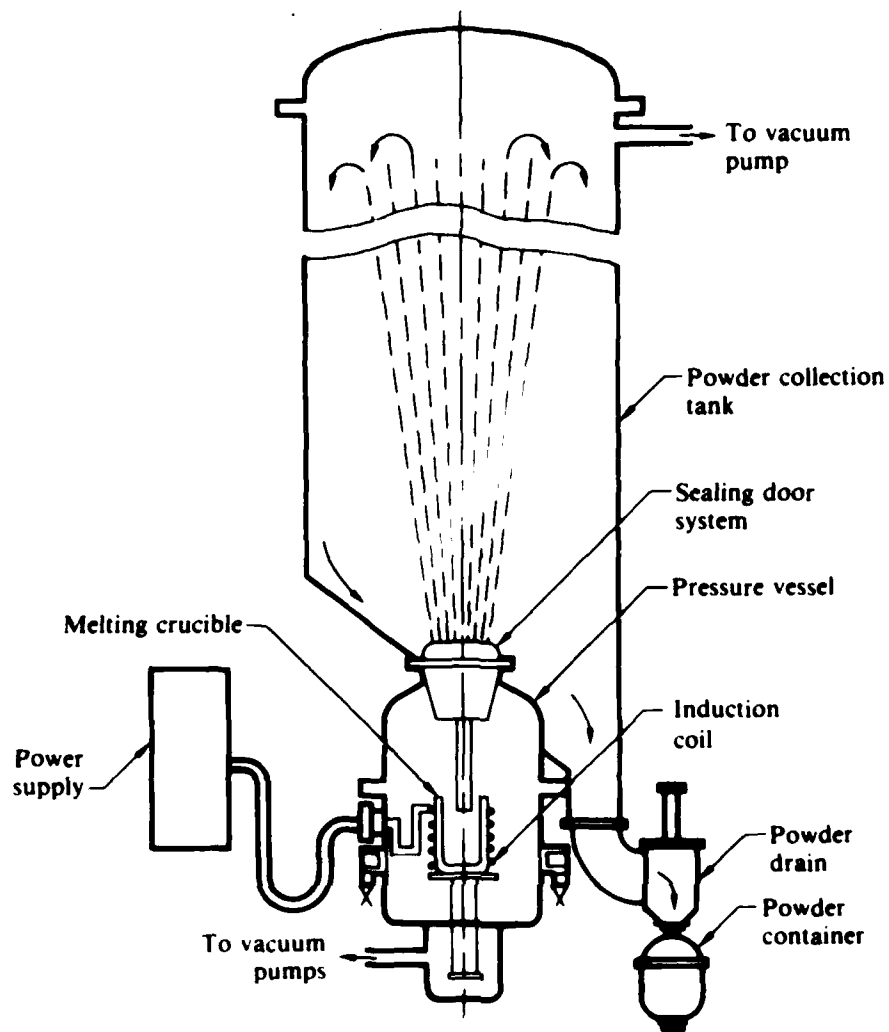
Three 35-kg lots of rapidly solidified 99.9% Al, Al-3Li-1Cu-1Mg-0.2Zr, and Al-8Fe-7Ce alloy powders were prepared by vacuum atomization at Homogeneous Metals, Inc., Clayville, NY, using the apparatus shown in Figure 1. Each alloy was induction melted in an argon-filled pressure chamber. Once the melt had been homogenized and heated to the desired temperature, the sealing door was opened and the melt ejected through a transfer tube into the evacuated powder collection chamber. The melt was atomized and solidified by the escape of the pressurizing gas; the resultant powder cascaded into a vessel which could be valved off from the chamber for further handling.

In addition to the above alloys, one kilogram of Al-8Fe-4Ce alloy powder prepared by air atomization at ALCOA Technical Center, PA, was procured from the Air Force Wright Aeronautical Laboratories-Materials Laboratory.

The nominal compositions and chemical analyses of the alloys are listed in Table 1.

3.2 Powder Characterization

Particle-size distributions of the as-solidified powders were obtained by sieving ~ 20 g samples through electroformed sieves according to ASTM E161-70. Because of the more precise tolerances and freedom from clogging and particle entrapment, the electroformed sieves produce particle-size distribution data superior to those obtainable using wire-woven sieves. Typical particle-size distributions by weight, plotted on probability paper, are shown in Figure 2 for different alloys. The weight-frequency plots show near log normal distributions of particle sizes for all three metals. The geometric mean sizes are 66 μm for aluminum and 94 μm for Al-3Li-1Cu-1Mg-0.2Zr and Al-8Fe-7Ce alloys. In all three alloys 80% of the particles are between 30 and 150 μm . This distribution is ideal because the size range assures efficient tap density and microstructural uniformity in consolidated forms. Furthermore, excessive oxide formation and the explosion hazard are minimized because of the absence of ultrafine particles.



CP41 1643 1 R

Figure 1. Vacuum atomization apparatus.

Table 1. Nominal compositions and chemical analyses of the materials studied.

Nominal compositions	Actual compositions
Al	99.9% Al
Al-3Li-1Cu-1Mg-0.2Zr	Al-2.92Li-1.0Cu-1.2Mg-0.22Zr
Al-8Fe-7Ce	Al-8.6Fe-7.19Ce
Al-8Fe-4Ce	ND

CP41 1643 10 R

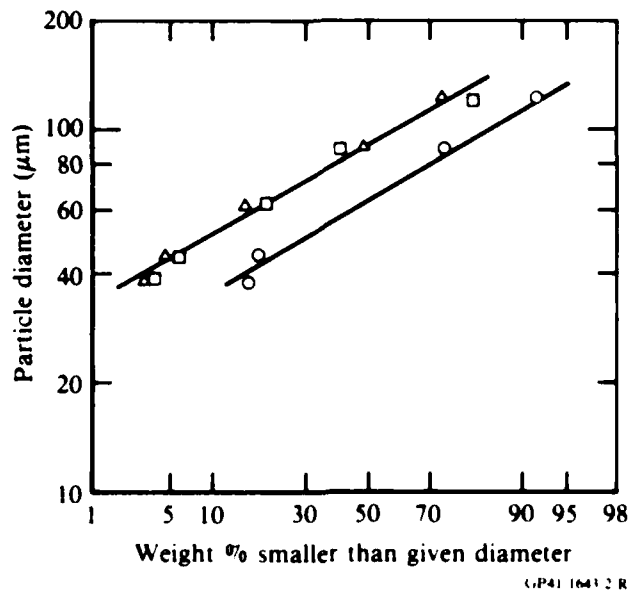


Figure 2. Particle size distributions of (○) aluminum, (△) Al-3Li-1Cu-1Mg-0.2Zr, and (□) Al-8Fe-7Ce powders.

The cooling rates of the powders were determined from dendrite-arm-spacing measurements. For the size ranges of 30-150 μm , the cooling rates were 10^4 - 10^3 K/s.

Scanning electron micrographs of typical powders are shown in Figure 3. The particles are spherical with dendritic and cellular microstructures over the entire range of particle sizes. Powder agglomerates such as those shown in Figure 3a are more numerous in Al than in the other alloy powders. The Al-8Fe-4Ce alloy powders produced by ALCOA have a large number of irregularly shaped particles.

The rapidly solidified powders were mounted in lucite and prepared for metallographic examination and microhardness measurements. The applied loads, indentation dimensions, and microhardness values are listed in Table 2. The hardness values of the Al-Li and Al-Fe-Ce alloys are about four times that of pure aluminum.

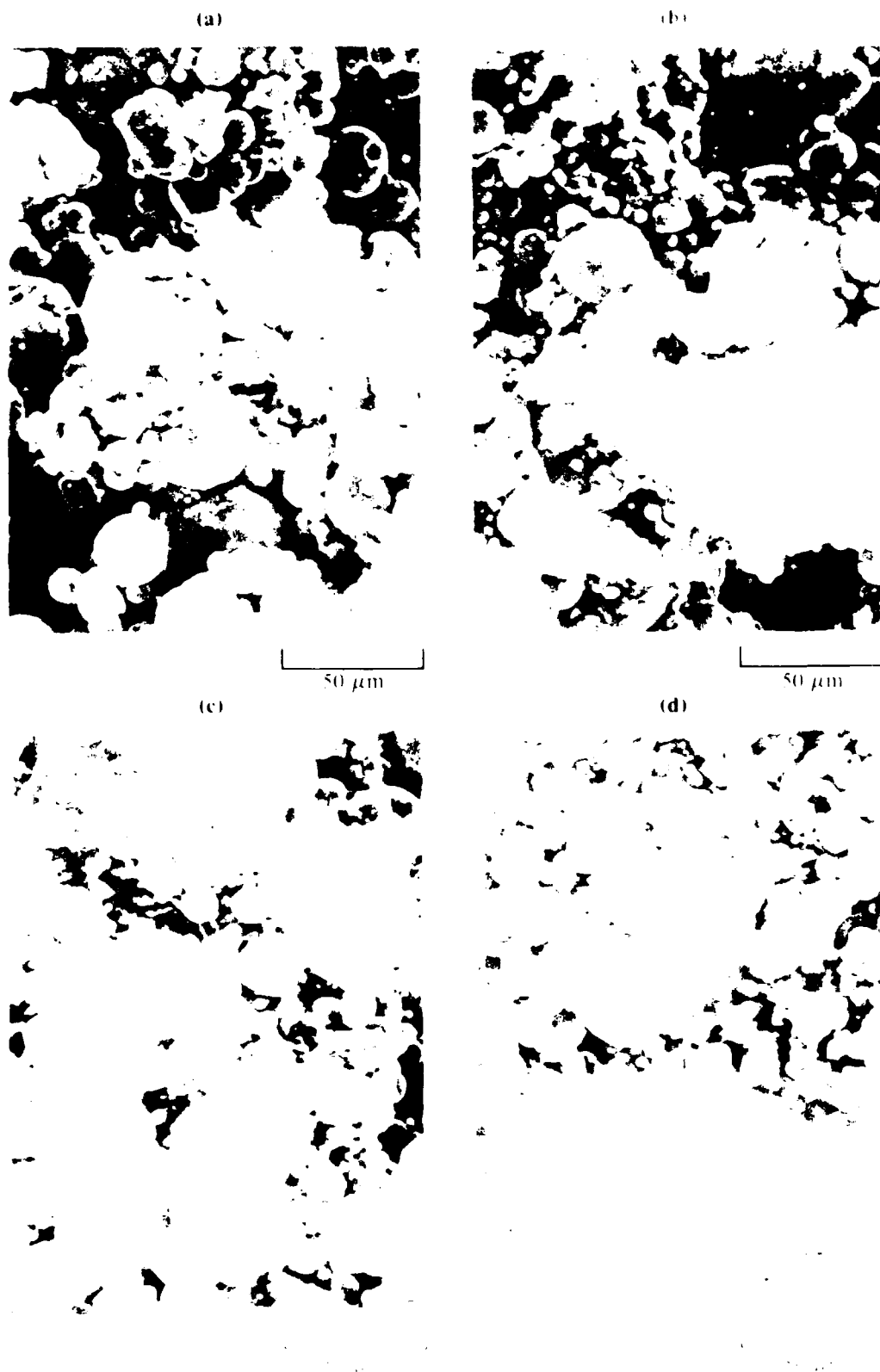


Figure 3. Scanning electron micrographs of rapidly solidified (a) 99.9% Al, (b) Al-3Fe-1Cu-1Mg-0.2Zr, (c) Al-8Fe-7Cu, and (d) Al-8Fe-4Cu powders.

Table 2. Indentation dimensions and microhardness values of powders studied.

Alloy	Applied load (g)	Mean indentation diagonal length* (μm)	Microhardness
Al	10	27.0	25.4
Al-3Li-1Cu-Mg-0.2Zr	10	14.0	94.6
Al-8Fe-7Ce	10	13.8	97.4
Al-8Fe-4Ce	15	16.9	97.4

*Average of 10 readings

GP41 1643 31 R

The phases present in the rapidly solidified and heat-treated samples were determined by x-ray diffractometry using monochromatic $\text{Cu K}\alpha$ radiation. For high-temperature anneals, the samples were enclosed in airtight stainless steel tubes, annealed at 400 and 500°C for 2 h, and cooled to 25°C in air. Figures 4-6 show the diffracted x-ray intensity peaks for the three alloys and the aluminum standard in the rapidly solidified and heat-treated conditions.

The rapidly solidified Al-3Li-1Cu-1Mg-0.2Zr alloy consists of predominantly Al-Li-Cu-Mg solid solution and a small volume fraction of Al_3Li (δ') precipitates. Upon annealing at 400 and 500°C, the equilibrium Al-Li and $\text{Al}_6\text{Li}_3\text{Cu}$ (T_2) phases are formed. However, because of the small volume fraction, these phases were not detected by x-ray diffraction. Transmission electron microscopy was used instead.

In the Al-Fe-Ce alloys, a large number of intensity peaks other than those of Al were observed even in the rapidly solidified condition, indicating phase separation during cooling. These additional peaks were more intense in the 400 and 500°C annealed alloys. In the Al-8Fe-4Ce alloys most of the additional peaks could be identified as $\text{Al}_3(\text{Fe,Ce})$ or $\text{Al}_6(\text{Fe,Ce})$. However, in the Al-8Fe-7Ce alloy, there were numerous peaks which could not be identified unambiguously. The interplanar spacings of the unidentified phases and the values previously reported for different phases in this system⁶ are given in Table 3.

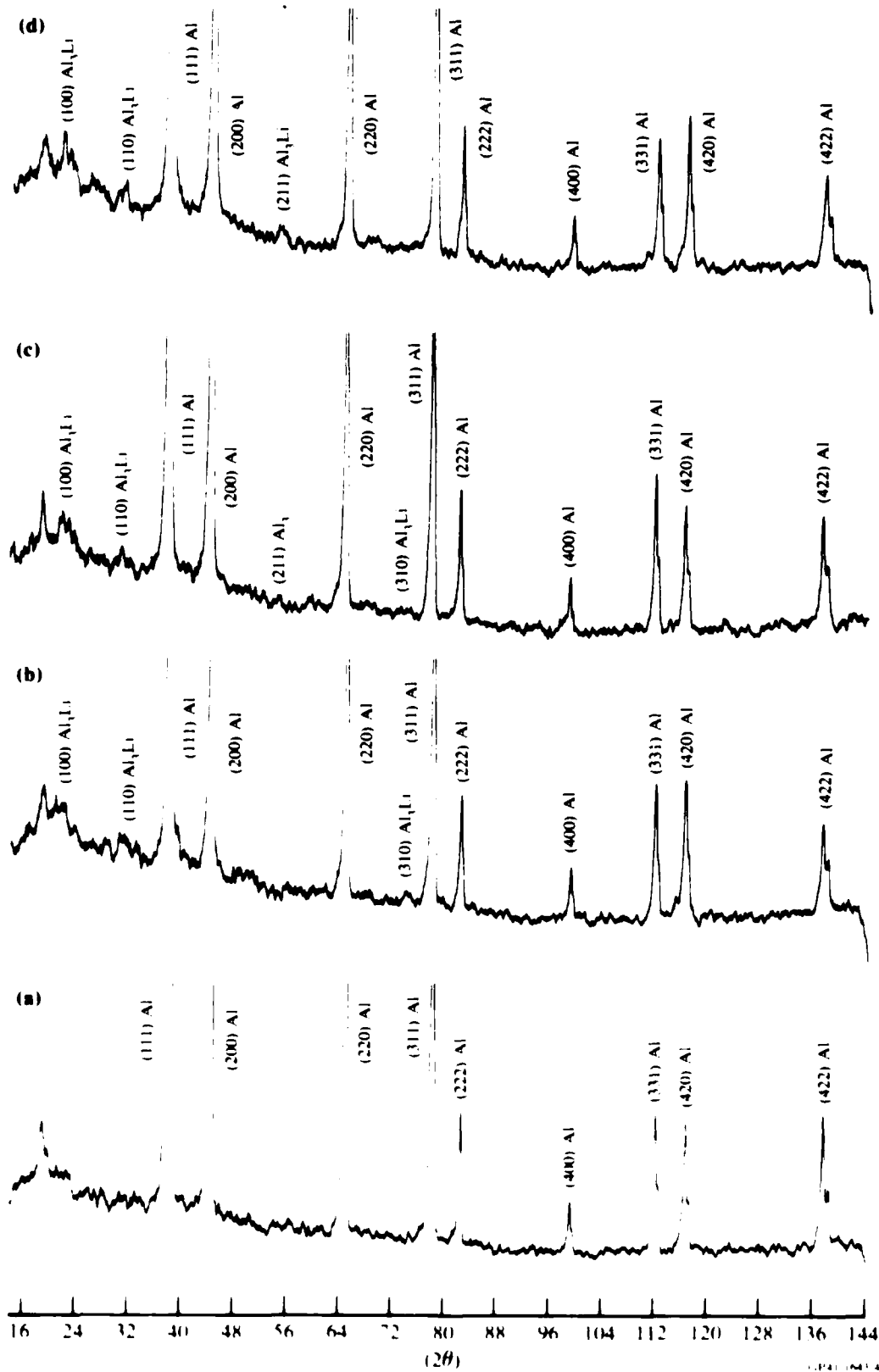


Figure 4. X-ray diffraction peaks of (a) aluminum, (b, c, and d) Al-31.1Cu-1Mg-0.2Zr alloy, (b) rapidly solidified, (c) annealed at 400°C for 2 h, and (d) annealed at 500°C for 2 h.

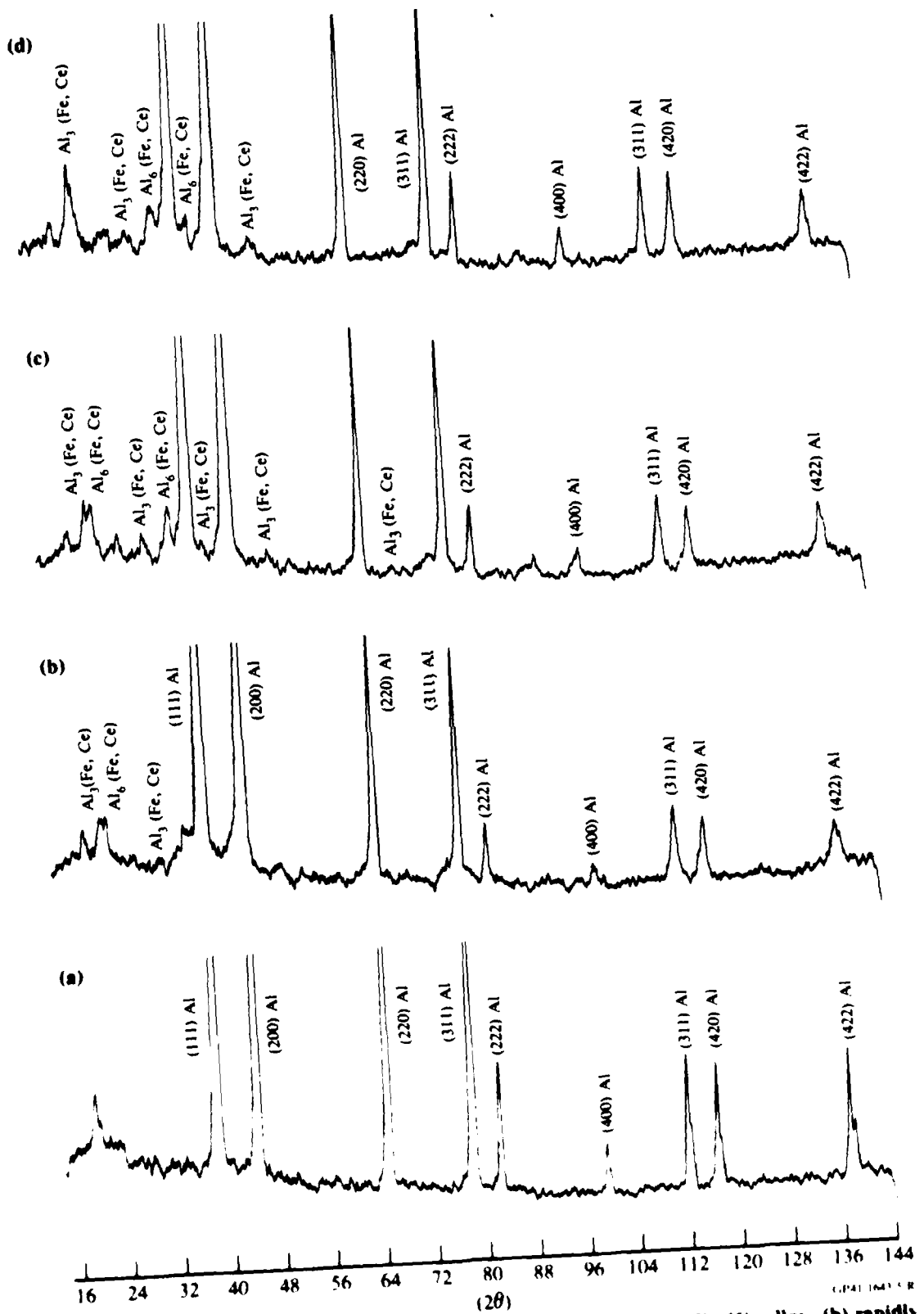


Figure 5. X-ray diffraction peaks of (a) aluminum, (b, c, and d) Al-8Fe-4Ce alloy, (b) rapidly solidified, (c) annealed at 400°C for 2 h, and (d) annealed at 500°C for 2 h.

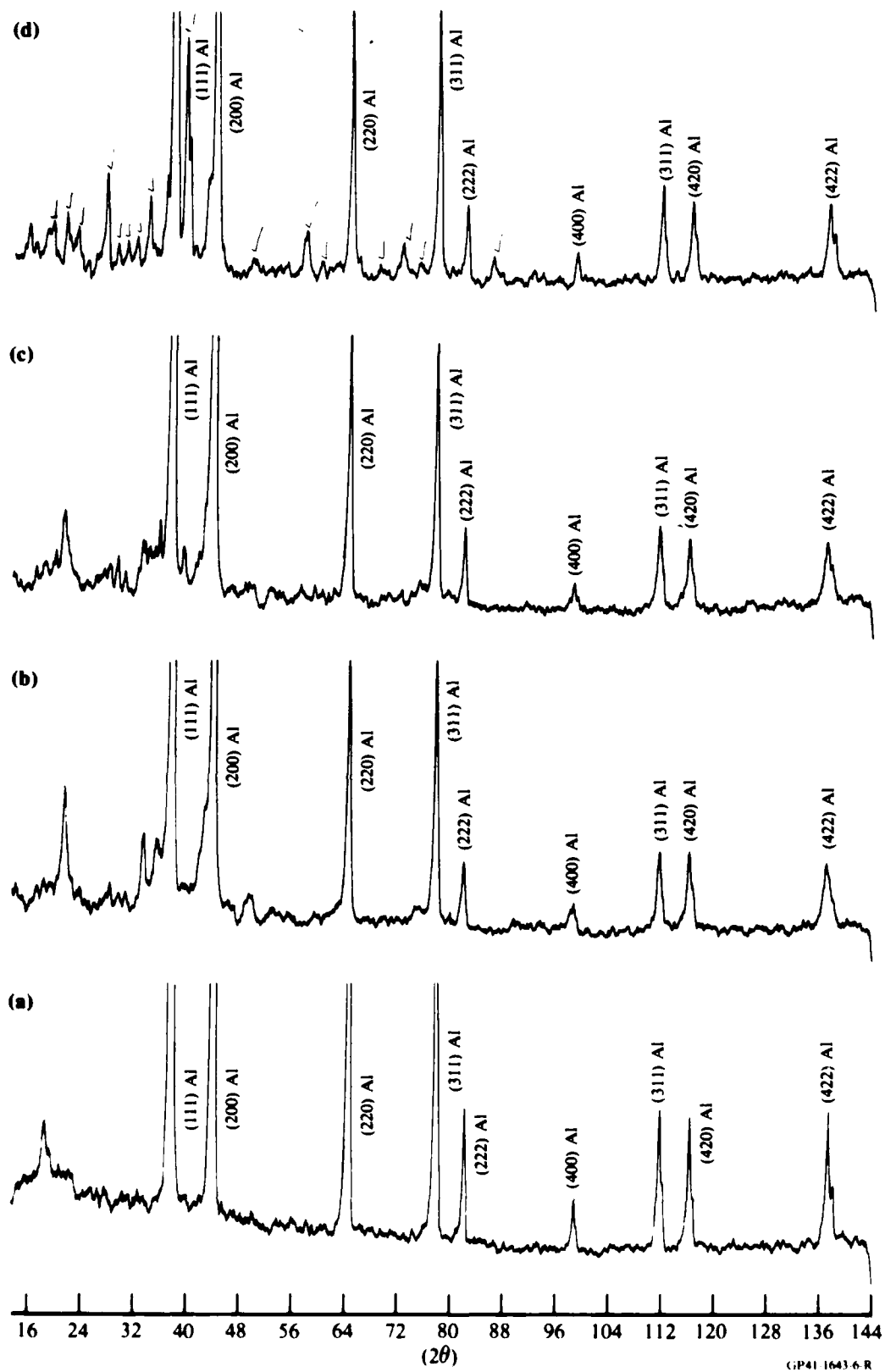


Figure 6. X-ray diffraction peaks of (a) aluminum, (b, c, and d) Al-8Fe-7Ce alloy, (b) rapidly solidified, (c) annealed at 400°C for 2 h, and (d) annealed at 500°C for 2 h.

Table 3. Interplanar spacing (d) of phases detected in Al-8Fe-7Ce alloy annealed at 500°C for 2 h.

d - spacings (nm) reported in reference	d - spacings (nm) determined in the present investigation
0.680	
0.540	0.54378
0.515	
0.445	0.44615
0.376	0.37697
0.319	0.31921
0.316	0.31699
0.300	0.30079
0.287	
0.275	
0.274	
0.260	0.26033
0.2425	0.24327
	0.23412
0.225	0.22539
0.222	0.22273
	0.20987
0.201	0.20251

GP41-1643-33-R

The evolution of volatile contaminants in the alloy powders was studied by mass spectroscopic analysis. Approximately 10-15 mg of alloy powder was heated from 25 to 500°C at the rate of 25-30°C per minute in the solid-sampling probe of the Vacuum Generator Model ZAB-3F mass spectrometer. The mass spectrometer was repetitively scanned over the mass range of interest as volatile materials evolved from the sample. The scan rate for the mass spectrometer was 5 s per decade of mass from 600 to 1 atomic mass units with a scan reset time of 2 s. Mass spectra so obtained were recorded with the aid of a data acquisition system and processed and analyzed after completion of a scan.

Figure 7 shows the ion intensity of hydrogen, water, oxygen, and carbon dioxide as a function of temperature for aluminum and the three aluminum alloys. Significant hydrogen evolution occurs at 400-500°C in aluminum and Al-8Fe-7Ce and at 350-400°C in Al-Li alloy. The hydrogen evolution is considerably less in Al-Fe-Ce alloys and occurs at a lower temperature of 300°C.

Almost all the water evolution occurs at 100-200°C in all the alloys. No significant differences in oxygen evolution was detected in the four alloys. Carbon dioxide evolution in all the alloys occurs at two temperature ranges--200-300°C and 500°C.

3.3 Consolidation of Aluminum Alloys Powders

3.3.1 Cold Compaction

The tap density of each alloy powder was determined by filling a 35-mm-diameter, 105-mm-long cylindrical steel container with 120 g of powder, vibrating the container for 24 h, and measuring the volume of the settled mass. Tap-densities are listed in Table 4. The smaller oxide thickness of pure aluminum particles results in high friction between particles and reduces interparticle sliding, which accounts for the low tap density of the aluminum powders. The Al-Li-Cu-Mg and Al-Fe-Ce alloys with thicker oxide films have reduced interparticle friction, increased interparticle sliding, and higher tap densities.

Cold compaction experiments were performed to determine the effects of pressure on bulk movement of particles as well as the deformation and fracture of particles, the two basic processes that contribute to densification during compaction. The powders were packed in a 12.5-mm-diameter cylindrical die and compacted in a 250-kN hydraulic load frame. The ratio of the height to the diameter of the powder compact was in all cases < 0.5 to insure uniform densification. The ram displacement as a function of applied load was monitored, and the linear displacement of the ram was used to calculate the density of the compact by assuming constancy of mass of the alloy and cross-sectional area of the compaction die.

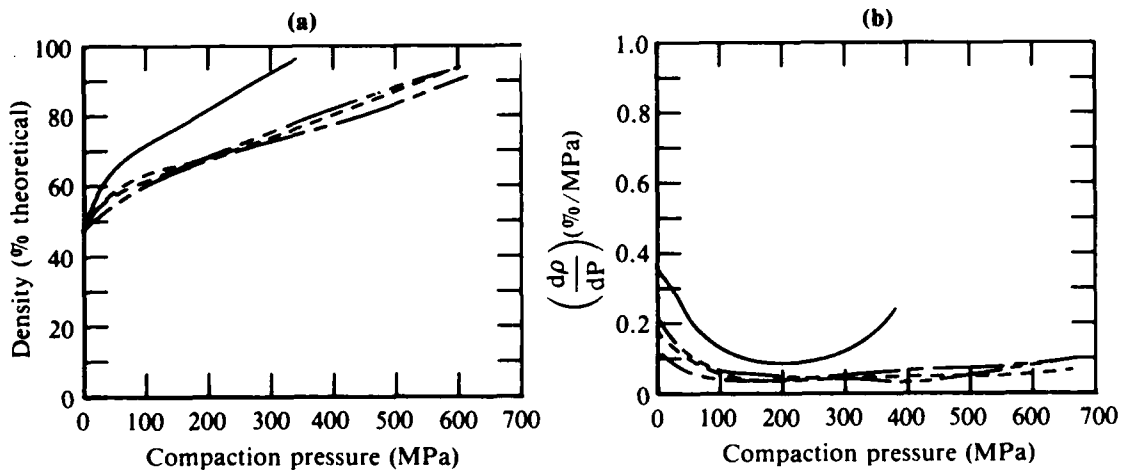
Table 4. Tap densities and theoretical densities of materials studied.

Alloy	Theoretical density (g/cm ³)	Tap density (g/cm ³)	Tap density (% theoretical density)
Al	2.7	1.41	52.0
Al-3Li-1Cu-1Mg-0.2Zr	2.484	1.6	64.4
Al-8Fe-4Ce	2.95	1.86	63.0
Al-8Fe-7Ce	2.994	2.0	66.9

GP41-1643-32-R

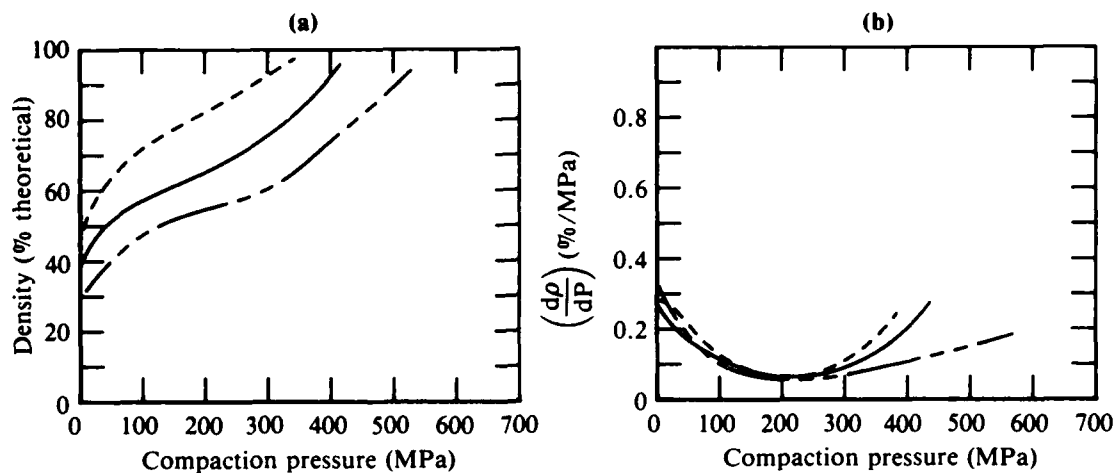
Densification of powder particles progresses in three stages during compaction as shown in Figures 8a and 8b. The first stage, in which density increases rapidly with pressure, involves the bulk movement of particles, usually referred to as transitional restacking. This stage is followed by a second in which the rate of change of density with pressure is constant. This second stage is dominated by the plastic deformation of the particles. The final stage of densification involves particle fragmentation and interparticle bonding. This last stage is more pronounced in aluminum because of its high ductility. The pressure required for complete densification is lower, the transitional restacking stage is longer, and the rate of density change with pressure is higher for pure aluminum than for the alloys.

In the transitional restacking stage of compaction, powder consolidation occurs by the movement of powder particles past one another and repacking. The amount of particle repacking that occurs during the transitional restacking stage further depends on the size and shape distributions of particles and the rate of pressure application. The effect of particle-size distribution on densification is shown in Figure 9, which indicates that powders with normal distributions and large standard deviations from the mean size (curve A in Figure 9a) can pack more closely than powders having a small standard devia-



GP41-1643-8-R

Figure 8. Variation with compaction pressure of (a) density and (b) rate of density change with pressure $\left(\frac{d\rho}{dP}\right)$ for (—) aluminum, (----) Al-3Li-1Cu-1Mg-0.2Zr, (- - -) Al-8Fe-4Ce, and (— - —) Al-8Fe-7Ce powders consolidated by uniaxial pressing at 25°C.



GP41-1643-9

Figure 9. Effect of powder-size distribution on (a) densification and (b) rate of density change with pressure $\left(\frac{dp}{dP}\right)$ of aluminum powders consolidated by uniaxial pressing at 25°C. Powder size ranges: (-----) 10-260 μm , (————) <38 μm , and (— · — · —) 125-180 μm .

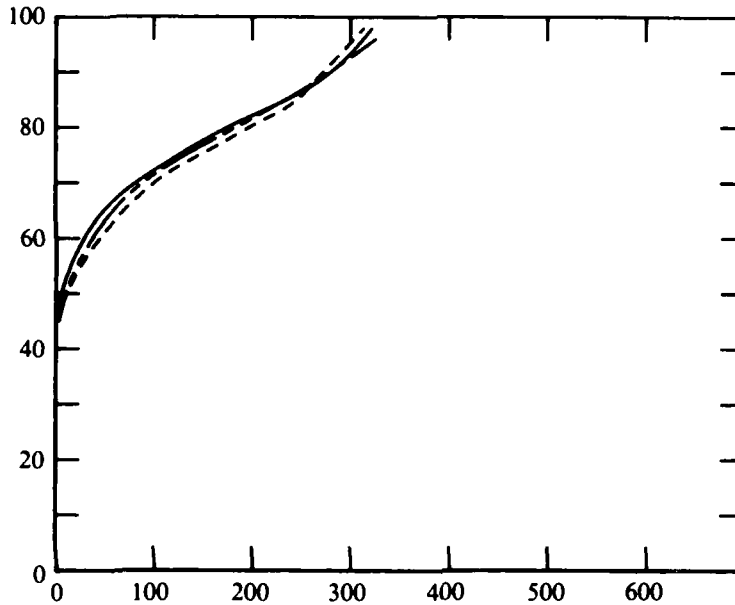
tion (curves B and C in Figure 9a) because of the ease with which small particles orient themselves into the interstices of groups of larger particles. The densification curves in Figure 10 indicate that the rate of pressure application has no significant effect on densification. However, very high rates of pressure application can cause premature immobilization of particles because high compressive stresses on the particles tend to block open passages.

Transitional restacking is followed by a compaction stage in which particles deform plastically to fill the voids in the powder compact. The pressure dependence of densification during this stage of compaction has been described by an empirical relation⁷

$$\ln \left(\frac{1}{1-\rho} \right) = k_1 P + k_2, \quad (1)$$

where ρ is the fraction of theoretical density of the powder, P is the compaction pressure, and k_1 and k_2 are constants. The constant k_1 is related to the yield strength σ_y of the constituent powder particles by the relation

$$k_1 = \frac{1}{3\sigma_y}, \quad (2)$$



GP41-1643-10-R

Figure 10. Effect of ram-displacement rate on densification of aluminum-powder compacts consolidated by uniaxial pressing at 25°C. Initial powder compact height is 1.75 cm, final powder compact height is 0.75 cm. Ram displacement rates: (— — —) 2.5×10^{-3} cm/s⁻¹, (— · — ·) 5.0×10^{-3} cm/s, and (————) 1.0×10^{-2} cm/s.

and k_2 is related to the powder size, morphology, and the degree of densification achieved during transitional restacking by the expression

$$k_2 = \ln \left(\frac{1}{1-\rho_0} \right) + B . \quad (3)$$

In Equation (3), ρ_0 is the relative density after transitional restacking, and B is a constant which decreases with decreasing particle size and increasing sphericity ($B = 0$ for spherical particles). Combining Equations (1), (2), and (3),

$$\ln (1-\rho) = [\ln (1-\rho_0) - B] - (P/3\sigma_Y) . \quad (4)$$

The density increases with increasing pressure, increasing relative density after transitional restacking, increasing values of B, and decreasing yield strength of the particle material.

The pressure dependence of densification calculated from Equation (4) is compared with experimentally determined values for Al and Al-Li-Cu-Mg-Zr

alloys in Figure 11. The equation does not correctly predict the pressure dependence of densification because work hardening of the powder particles is not included in the above treatment.

An accurate description of the pressure dependence of densification should take into account the porosity of the compact, and the pressure P in Equation (4) should be replaced by an effective stress σ_{eff} which is the applied load divided by the contact area projected in a plane normal to the applied load, which is a fraction of the cylindrical die face area.

Figure 12 shows plots of $\ln p$ as a function of $\ln (\sigma_{\text{eff}}/Y)$ for Al and Al-3Li-1Cu-1Mg-0.2Zr. Based on the microhardness values of the powders and available tensile data for solution-annealed alloys, yield stress values of 56 and 224 MPa were assumed for Al and Al-3Li-1Cu-1Mg-0.2Zr, respectively. The densification curves shown in Figures 12a and 12b follow the same trend observed for the plastic deformation of Al and Al-3Li-1Cu-1Mg-0.2Zr.

Microstructures of aluminum powder compacts are shown in Figures 13-18. In aluminum powder compacts significant plastic deformation ($> 50\%$ plastic strain) of powder particles is observed. Close to 99% of theoretical density could be obtained by cold compacting Al powder. The apparent lack of inter-particle bonding in Figure 13 is due to heavy etching of the compact for scanning electron microscopic examination. The Al-3Li-1Cu-1Mg-0.2Zr alloy shows a larger number of voids and less plastic deformation than in Al. In agreement with the high work-hardening exponent observed, Al-8Fe-7Ce exhibits the lowest density ($\approx 96\%$ of theoretical density) and the least amount of plastic deformation.

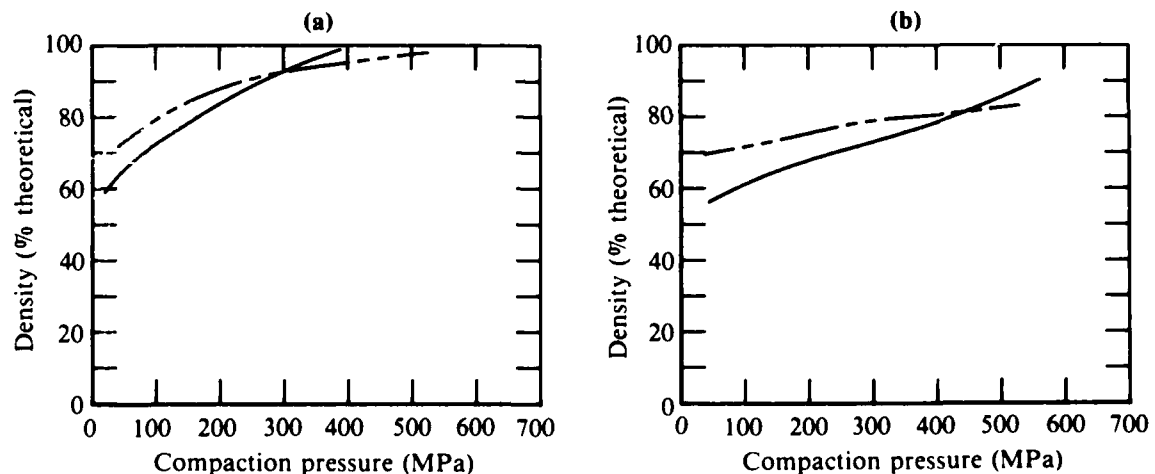
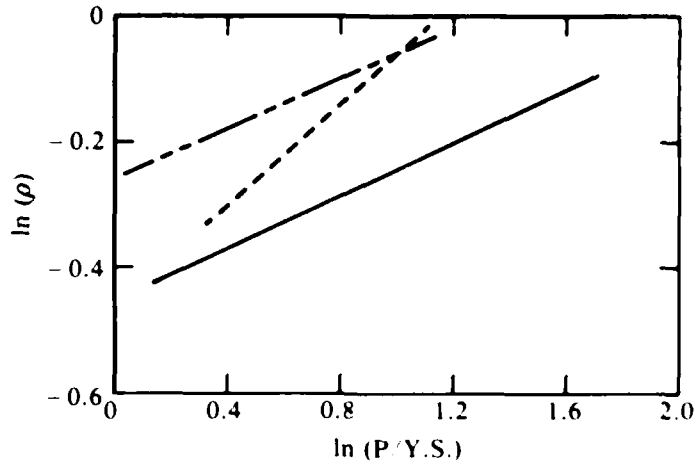
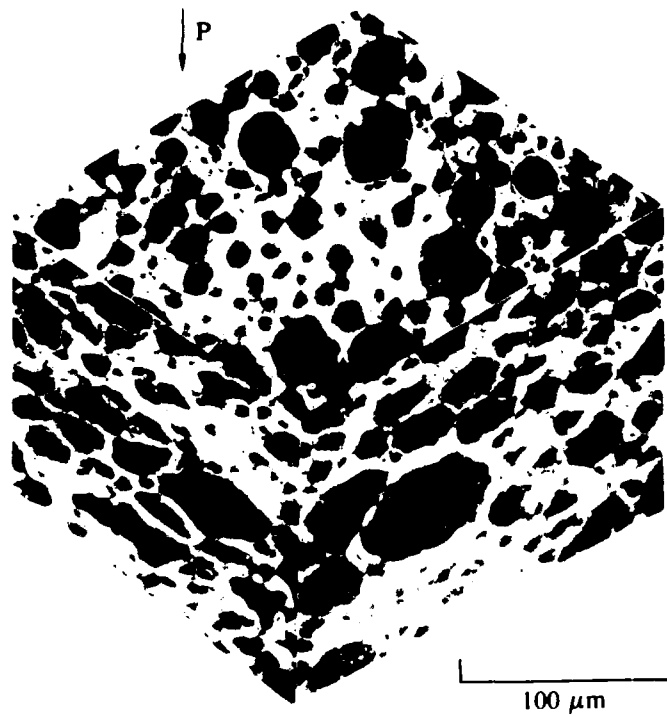


Figure 11. Variation of density with compaction pressure for (a) aluminum and (b) Al-3Li-1Cu-1Mg-0.2Zr alloy powders consolidated by uniaxial pressing at 25°C: (---) experimental values and (—) calculated from Equation (4).



GP41 1643 12 R

Figure 12. Variation of \ln (density) with \ln (pressure/yield stress) for (—) aluminum, (- - - -) Al-3Li-1Cu-1Mg-0.2, and (- · - · -) Al-8Fe-7Ce alloy powders.



GP41 1643 13 R

Figure 13. Scanning electron micrographs of aluminum-powder compacts consolidated by uniaxial pressing at 25°C.

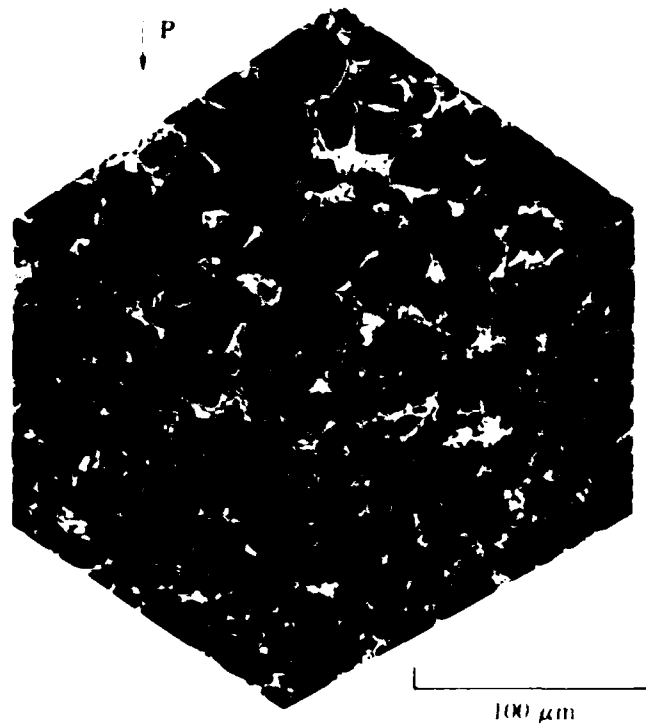


Figure 14. Scanning electron micrographs of aluminum-powder compacts (with $< 38\text{-}\mu\text{m}$ -diam powders) consolidated by uniaxial pressing at 25°C .

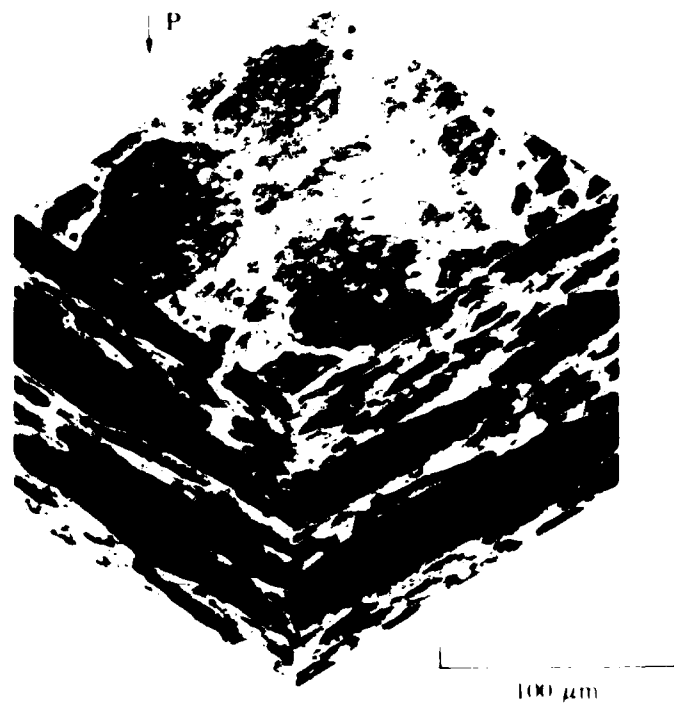


Figure 15. Scanning electron micrographs of aluminum-powder compacts (with 125 to $180\text{-}\mu\text{m}$ -diam powders) consolidated by uniaxial pressing at 25°C .

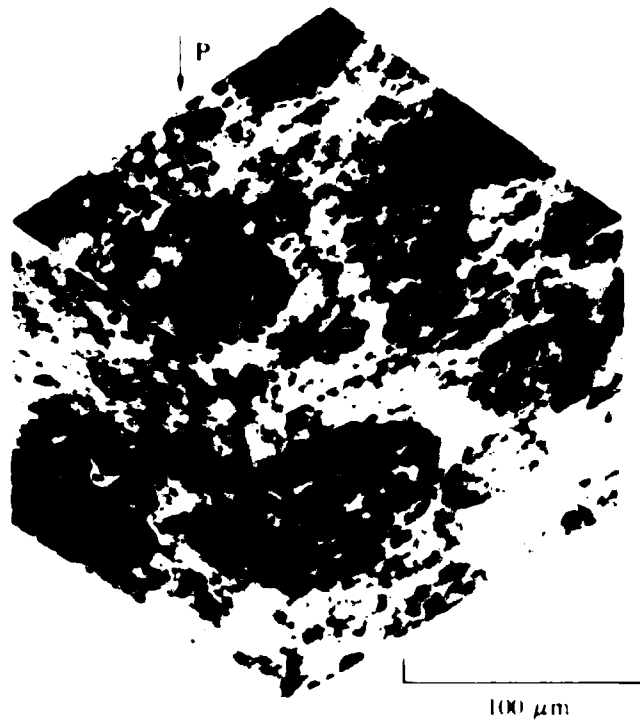


Figure 16. Scanning electron micrographs of Al-3Li-1Cu-1Mg-0.2Zr alloy powder compacts consolidated by uniaxial pressing at 25°C.

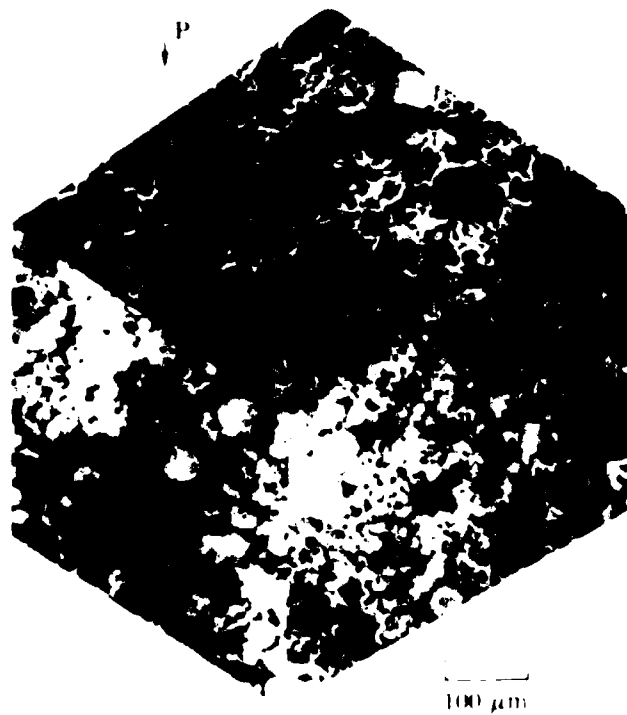


Figure 17. Scanning electron micrographs of Al-8Fe-7Ce alloy powder compacts consolidated by uniaxial pressing at 25°C.

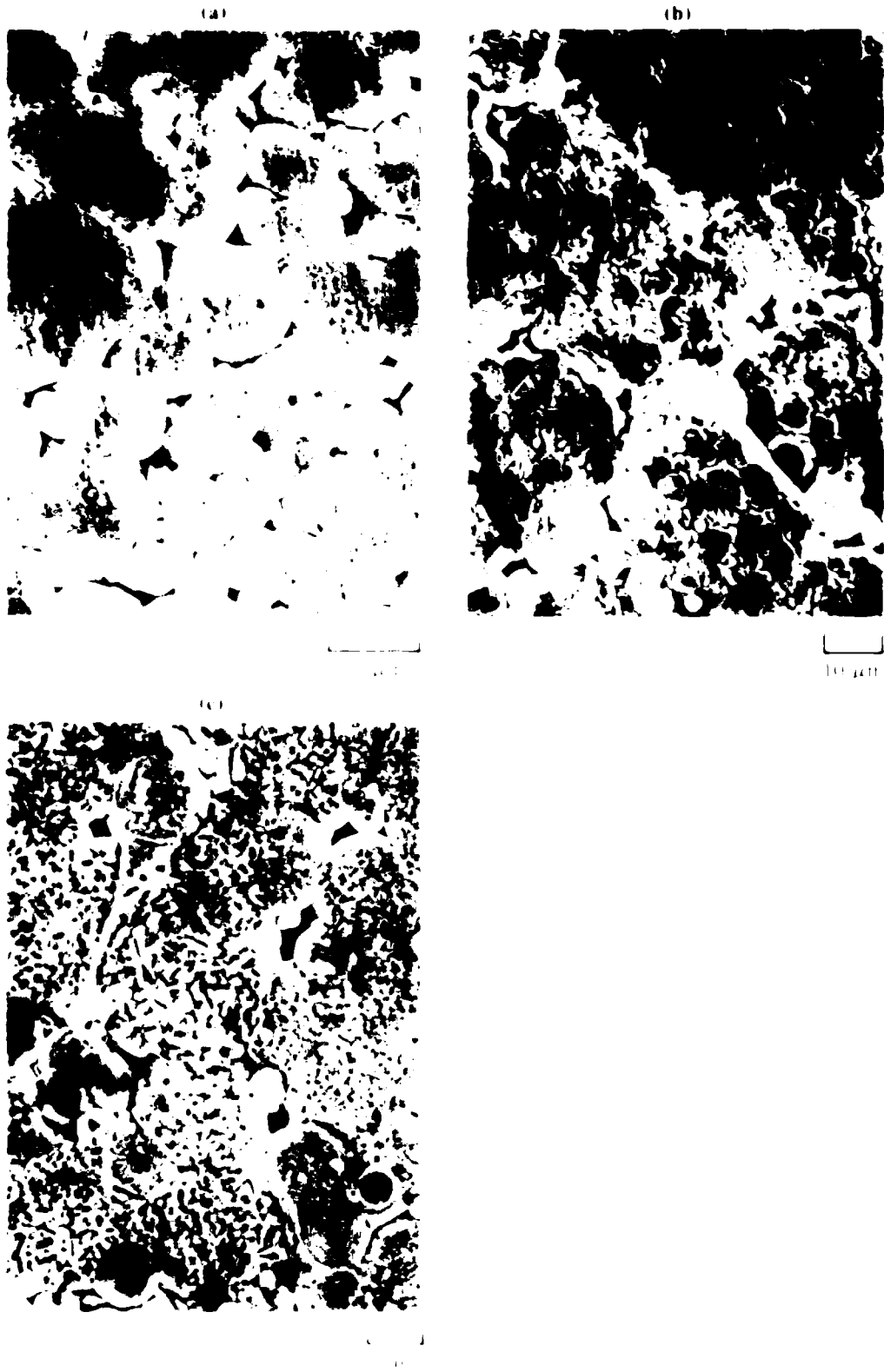


Figure 18. High magnification electron micrographs of (a) aluminum, (b) Al-3%Cu-1%Mg-0.2%Zr, and (c) Al-8%Fe-7%Cu alloy powder compacts consolidated by uniaxial pressing at 25 °C.

4. HIGH TEMPERATURE CONSOLIDATION AND EXPLOSIVE CONSOLIDATION OF RAPIDLY SOLIDIFIED ALUMINUM ALLOYS

4.1 Vacuum Outgassing

The effect of vacuum outgassing on hydrogen content was investigated. Outgassing was performed with the objective of extending a narrow range of the hydrogen content of the extrusion, which is important because of its effect on fracture toughness,⁷ and also the only gas-bearing measurable constituent of aluminum. It has been shown⁷ that significant hydrogen evolution occurs at 400-500°C in aluminum and at 200-300°C in the Al-Fe alloy. The hydrogen evolution is consistently less in Al-Fe-Fe and occurs at a lower temperature (300°C). Hence, powders of all three alloys were outgassed at 400 and 500°C at an active vacuum of 0.01 Pa for 2 h and were analyzed for hydrogen content by the permeation method (see Sect. 4.1.1). Table 5 lists the bulk hydrogen concentration for each alloy for the following three pretreatments: no outgassing, outgassing at 400°C, and outgassing at 500°C. While Al and Al-Fe-Fe have low concentrations of hydrogen, in contrast, the Al-Fe alloy without outgassing has a high concentration of hydrogen (120 ppm). Outgassing at 400 and 500°C considerably decreases the hydrogen, but it still remains at unacceptably high values.

4.2 Hot Pressing

Preliminary hot pressing experiments at 400°C were performed with 10 mm diameter cylindrical dies using alumina pans. The powders were first out-

Table 5. Bulk hydrogen and oxygen concentrations of PM aluminum alloys before and after vacuum outgassing.

Alloy	Vacuum outgassing temperature (°C)	Hydrogen concentration (ppm)		Oxygen concentration (%)	
		before	after	before	after
		Al	500	74	58, 51
Al-8Fe-7Ce	400	0.5	49, 14	0.087, 0.088	0.061, 0.051
Al-3Li-1Cu-1Mg-0.2Zr	500	150	36, 17	0.293, 0.296	0.008, 0.032

87-224-79

compacted to 4.4% of the theoretical density. The compacts were then pressed between two platens of a furnace mounted on a hydraulic press. After the compact and the platens were heated to the desired temperature, pressure application was begun. These samples were compacted at constant pressure, and the time dependence of compact formation was determined from the hydraulic ram displacement.

Figures 19 and 20 show the micrographs of Al, Al-10%Zn, Al-Mg-1.0%Zn, and Al-10%Zn-1.0%Mg compacts. The compacts were prepared with large initial particle diameters of 10-20 μ m. The grain structure of Al, however, Al-Zn, and Al-Mg-1.0%Zn compacts was characterized by small grain sizes.

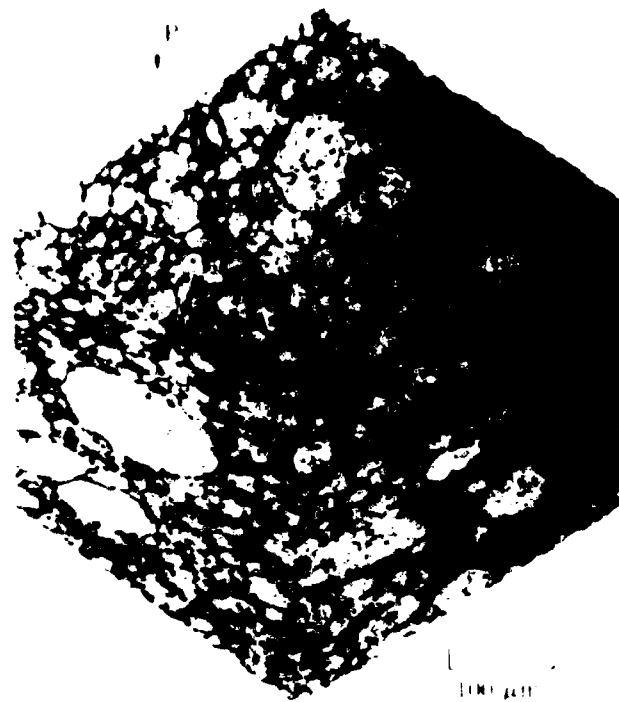
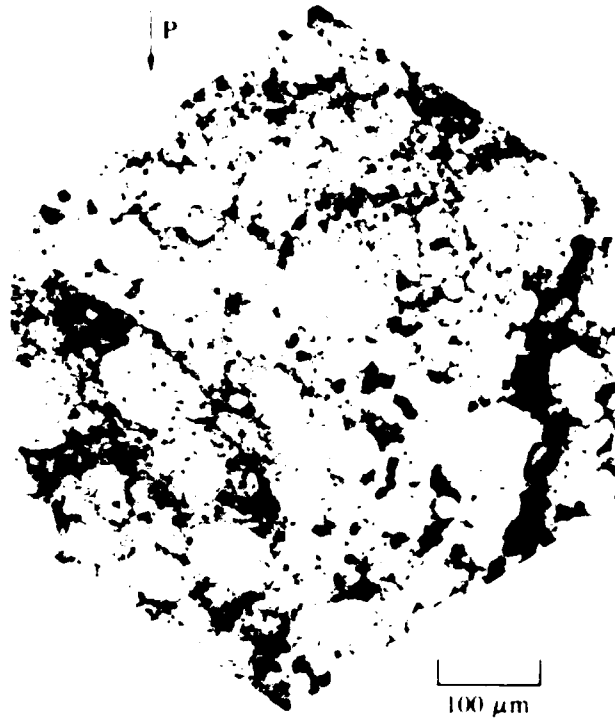
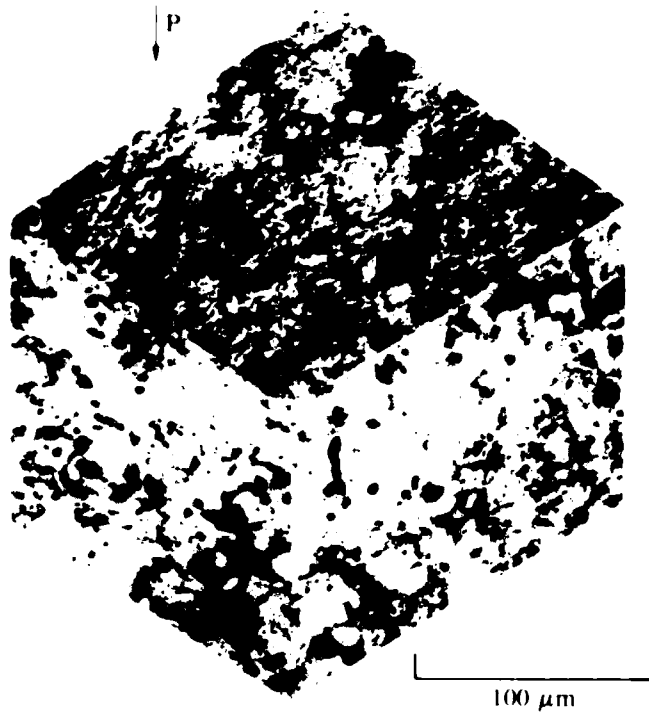


Figure 19. Optical micrographs of aluminum powder compacts consolidated by uniaxial pressing at 400 °C.



CP41-1643-20-R

Figure 20. Optical micrographs of Al-31i-10u-1Mg-0.2Zr alloy powder compacts consolidated by uniaxial pressing at 400°C.



CP41-1643-21-R

Figure 21. Optical micrographs of Al-8Fe-7Ce alloy powder compacts consolidated by uniaxial pressing at 400°C.

With the objectives of determining interrelationships between material flow properties and extrusion process variables and selecting extrusion process variables for large-size powder extrusions, laboratory-scale extrusions were prepared and evaluated.

Extrusions were performed in shear faced dies without lubrication. Dies were 50-mm long with a 19-mm diameter entrance hole. A wall thickness of 10-mm was necessary to prevent bulging during extruding. Exit hole diameters of 6.3, 4.75, and 3.2 mm yielded extrusion ratios of 9:1, 16:1, and 36:1, respectively. Alumina extrusion rams had typical wall clearances of 0.05 mm to reduce friction. Samples were extruded in a 225-kN (55 000-pound) electrohydraulic load frame using a 150-mm long collector tube. Samples were extruded at a constant ram velocity, and values of ram displacement and ram force were continuously recorded. The load-displacement plots were converted to plots of mean flow stress as a function of strain rate, where the mean flow stress is expressed as

$$\bar{\sigma} = \frac{P}{A_0 \ln \left(\frac{A_i}{A_0} \right)}, \quad (5)$$

where P is the ram load, A_0 is the initial cross-sectional area of the billet, and A_i is the final cross-sectional area after extrusion.

The strain rate is defined as

$$\dot{\epsilon} = \frac{3\sqrt{2} v d_0^2 \ln (d_0/d_i)^2}{d_0^3 - d_i^3}, \quad (6)$$

where v is the ram velocity, d_0 is the diameter of the billet, and d_i is the diameter of the extruded product. It is assumed that in the unlubricated shear-faced dies, the dead-metal zone makes an angle of 45° with the axis of the cylinder.

The extrusion rate dependences of flow stress for Al and Al-Li-Cu-Mg-0.2Zr extruded at 400°C are shown in Figure 23. At extrusion rate < 0.04 cm/s, flow stress is insensitive to extrusion rate in aluminum, but at larger extrusion rates, the flow stress increases with extrusion rate with a rate sensitivity

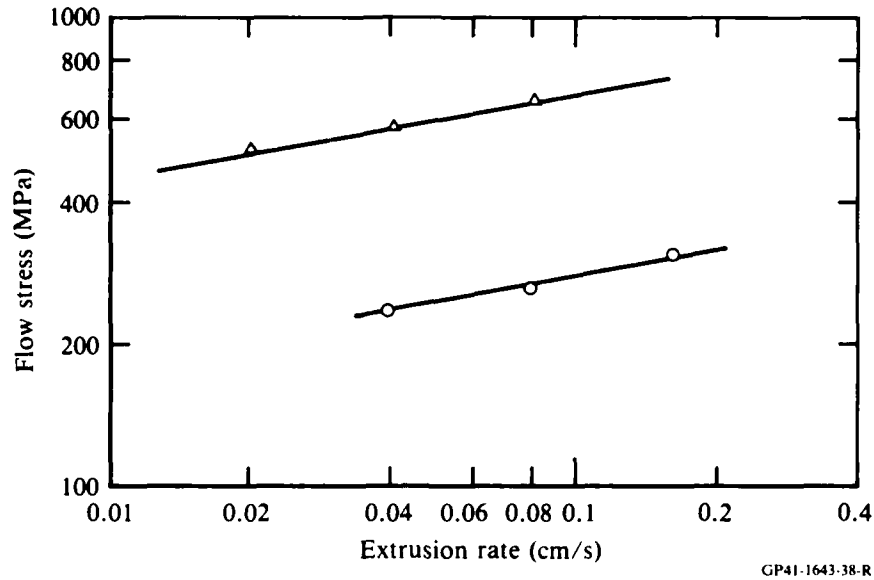
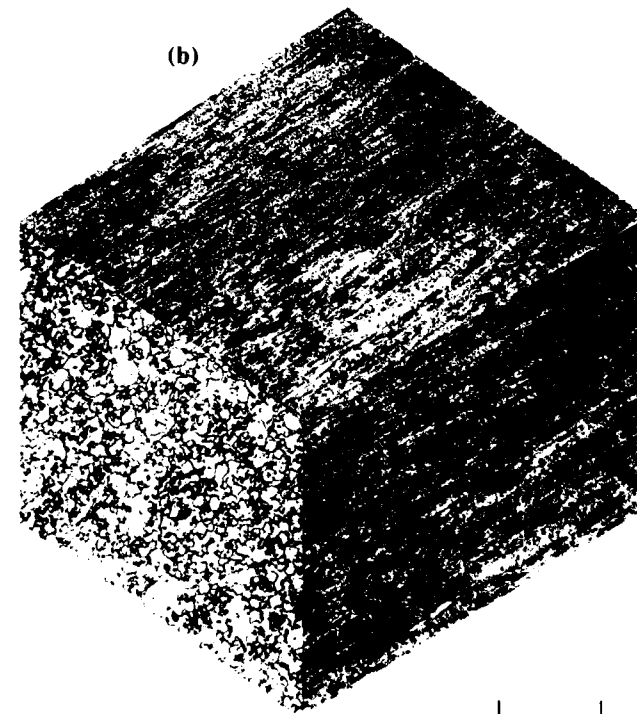
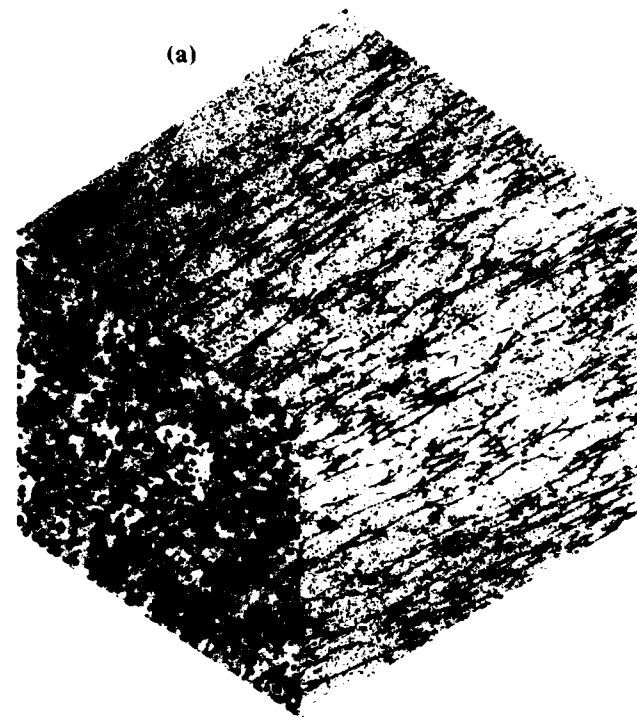


Figure 23. Variation of flow stress with extrusion rate of (○) aluminum and (△) Al-3Li-1Cu-1Mg-0.2Zr powders extruded at 400°C.

of 0.2. The Al-Li-Cu-Mg-Zr alloy, however, exhibits rate sensitivity = 0.2 at all extrusion rates from 0.02 to 0.16 cm/s.

The microstructures of aluminum powder compacts extruded at 400°C at ram displacement rates of 0.01, 0.04, 0.08, and 0.16 cm/s are shown in Figures 24a-24d. The specimen extruded at 0.01 cm/s has large numbers of voids at the interparticle boundaries. The powder particles are elongated in the extrusion direction. The original particle boundaries are clearly seen, indicative of poor interparticle bonding. The microstructure resembles that of a hot-pressed Al powder compact (compare Figures 24a and 19). In specimens extruded at higher displacement rates, complete interparticle bonding occurred without any trace of prior interparticle boundaries. Dynamic recrystallization resulted in recrystallized grain structures with grains elongated in the extrusion direction. The grain size in the plane perpendicular to extrusion direction decreases from ~ 10 μm at 0.04 cm/s to ~ 5 μm at 0.16 cm/s.

The Al-Li-Cu-Mg-Zr alloy extruded at 0.02 cm/s shows the original particle boundaries and the dendritic and cellular microstructure similar to those observed in hot-pressed alloy (Figure 25a). However, the specimen extruded at 0.08 cm/s reveals complete bonding without any evidence of interparticle boundaries (Figure 25b). In contrast to the recrystallized microstructures observed in Al, the Al-Li based alloy exhibits a recovered microstructure.



100 μm

GP41 1643 23 R

Figure 24. Optical micrographs of aluminum powder compacts extruded at 400°C at extrusion rates of (a) 0.01 cm/s, (b) 0.04 cm/s, (c) 0.08 cm/s, and (d) 0.16 cm/s.

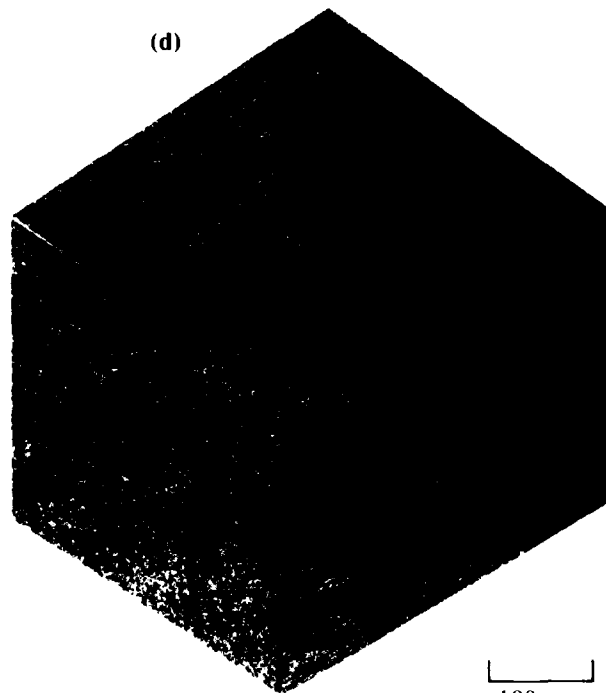
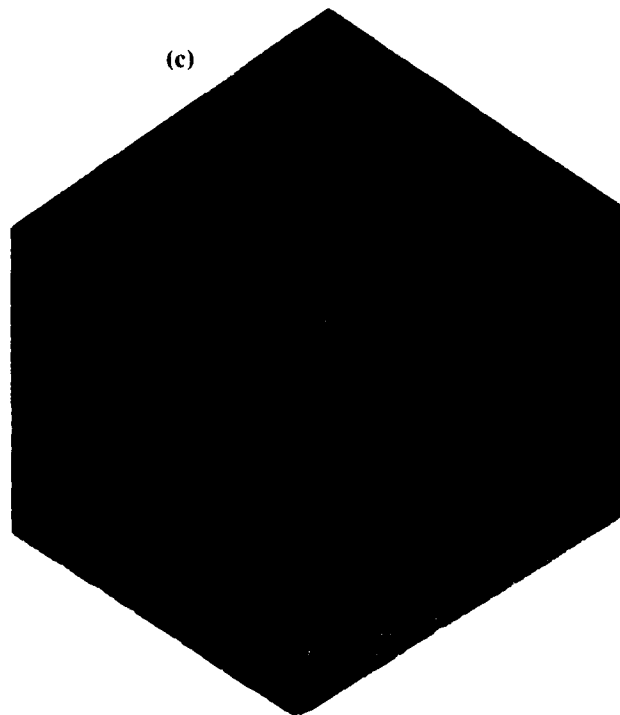
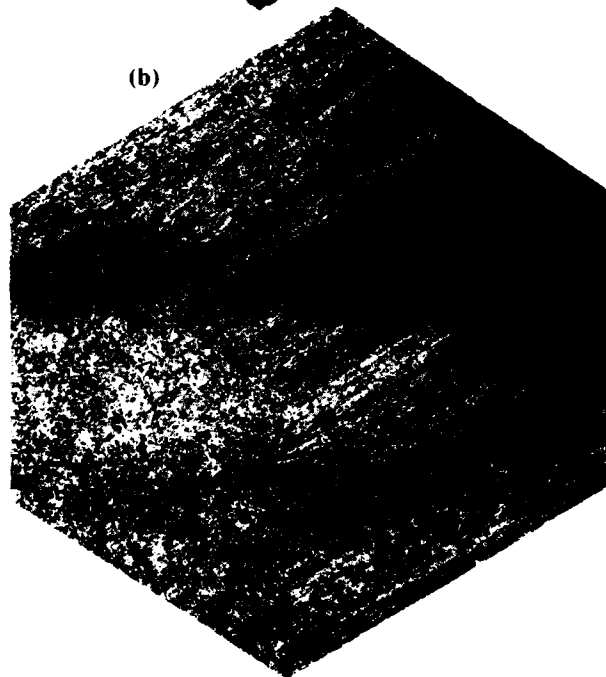
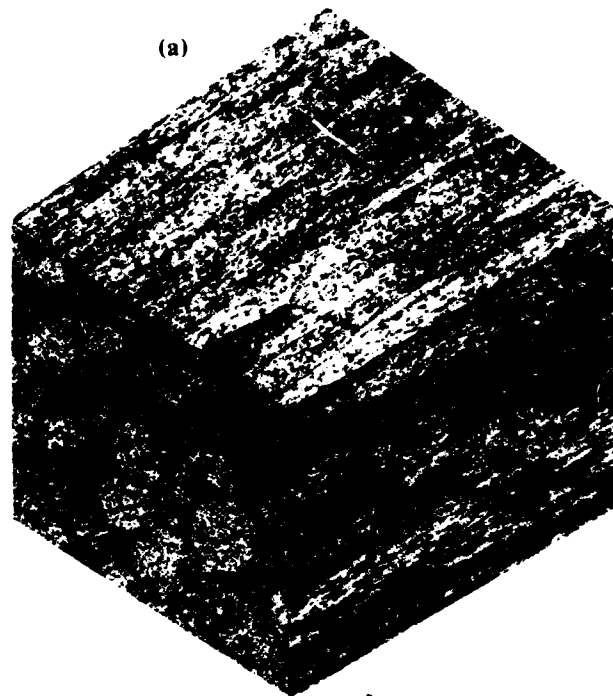


Figure 24. (Concluded)

GPO 164339

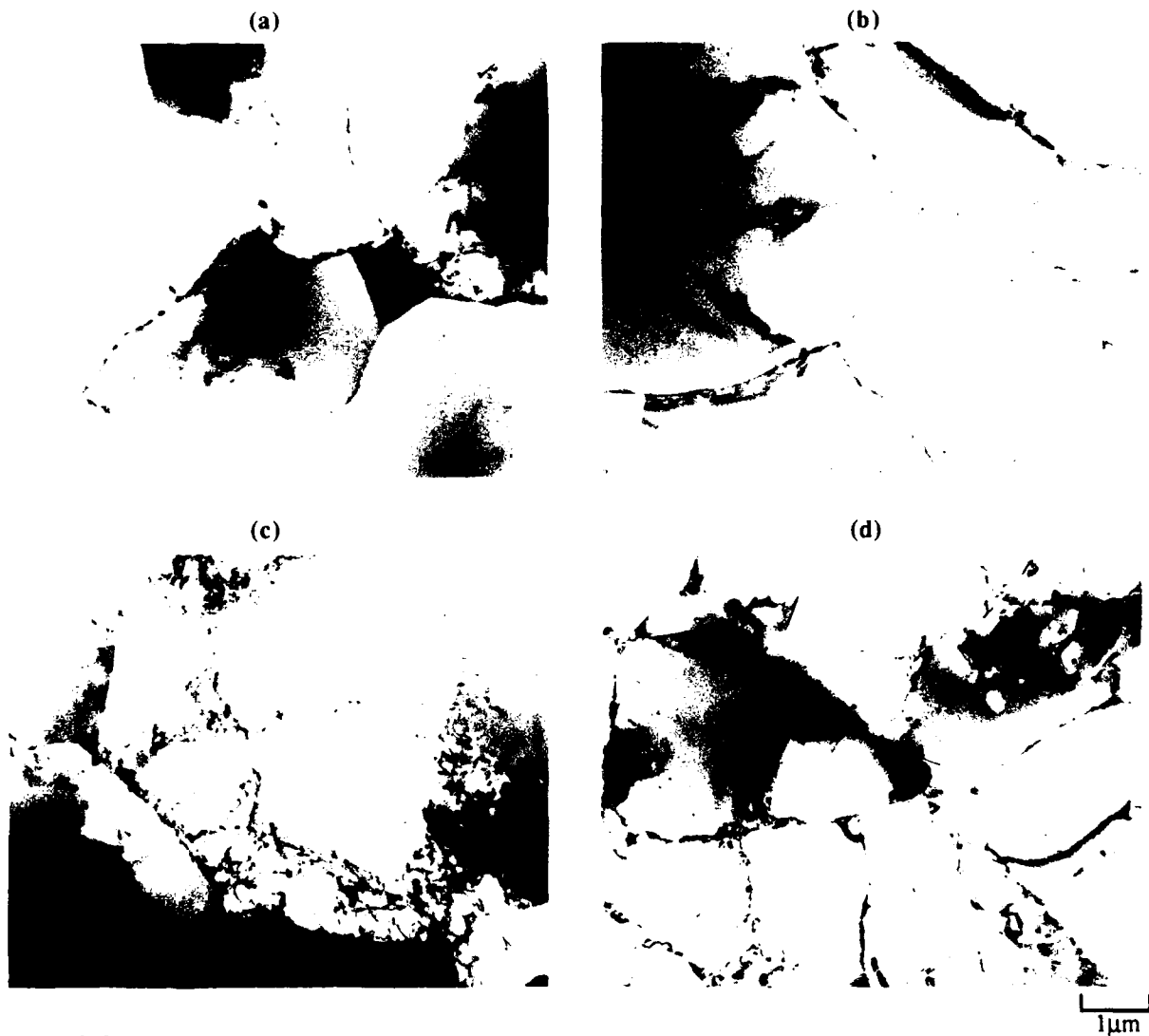


100 μm

GP41-1643-24-R

Figure 25. Optical micrographs of Al-3Li-1Cu-1Mg-0.2Zr alloy powder compacts extruded at 400°C at extrusion rates of (a) 0.02 cm/s and (b) 0.08 cm/s.

Transmission electron micrographs of Al and Al-3Li-1Cu-1Mg-0.2Zr extruded at different temperatures, strain rates, and reduction ratios are shown in Figures 26-35. In Al, the dislocation cell size increases with increasing extrusion temperature and decreasing strain rate, with typical cell sizes being 1-3 μm ; vacuum outgassing has no effect on the microstructure of extrusions. Al-3Li-1Cu-1Mg-0.2Zr alloy develops a fine (0.5- to 1.0- μm diameter) dislocation substructure, whose cell size is independent of extrusion temperature and strain rate. Al-3Li-1Cu-1Mg-0.2Zr specimens extruded without vacuum

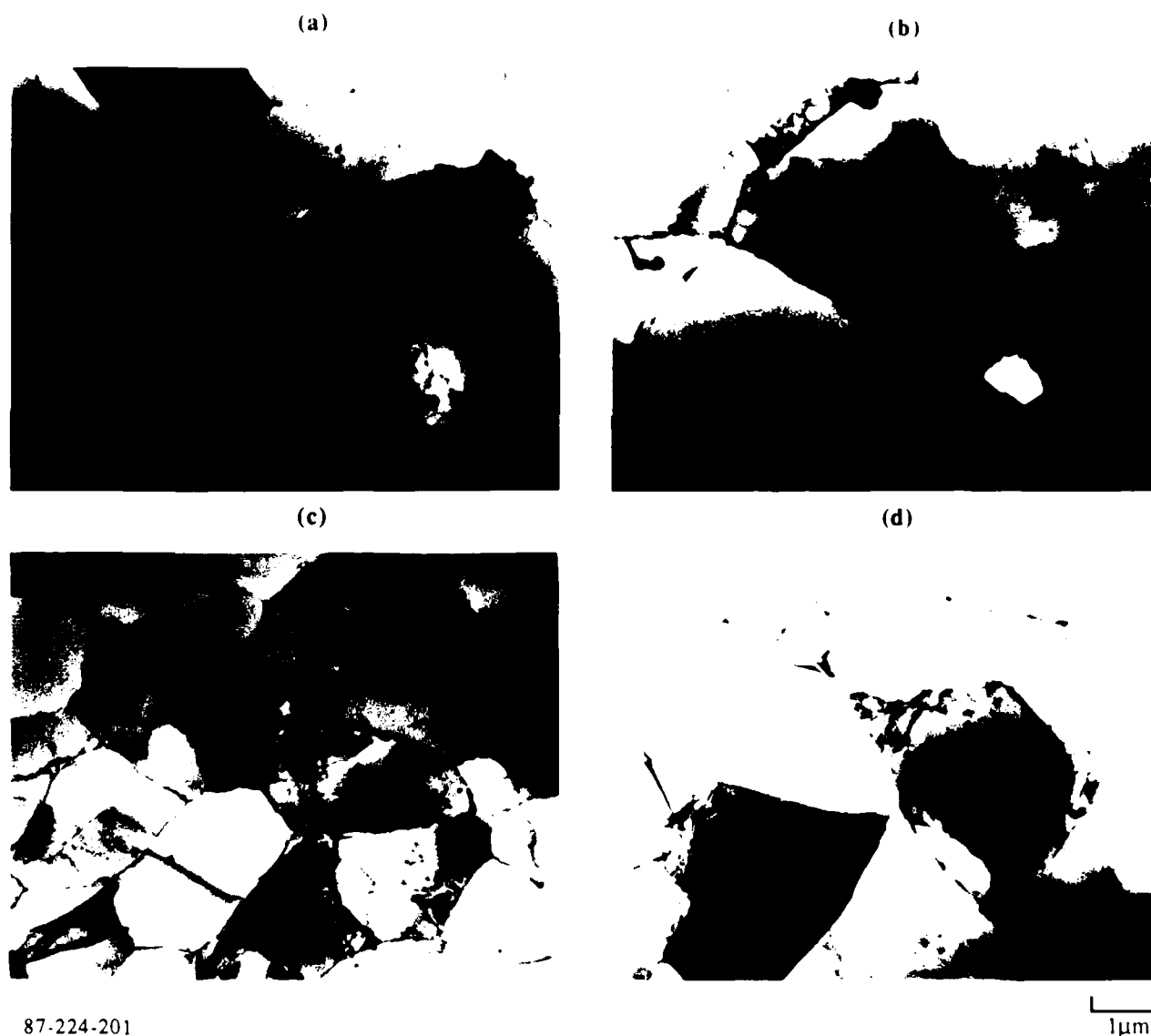


87-224-210

Figure 26. Transmission electron micrographs of 99.99% Al powders extruded at 350°C with an area reduction of 16:1. (a,b) vacuum outgassed at 500°C, (c,d) without vacuum outgassing; (a,c) strain rate of 1.59/s, (b,d) strain rate of 0.23/s.

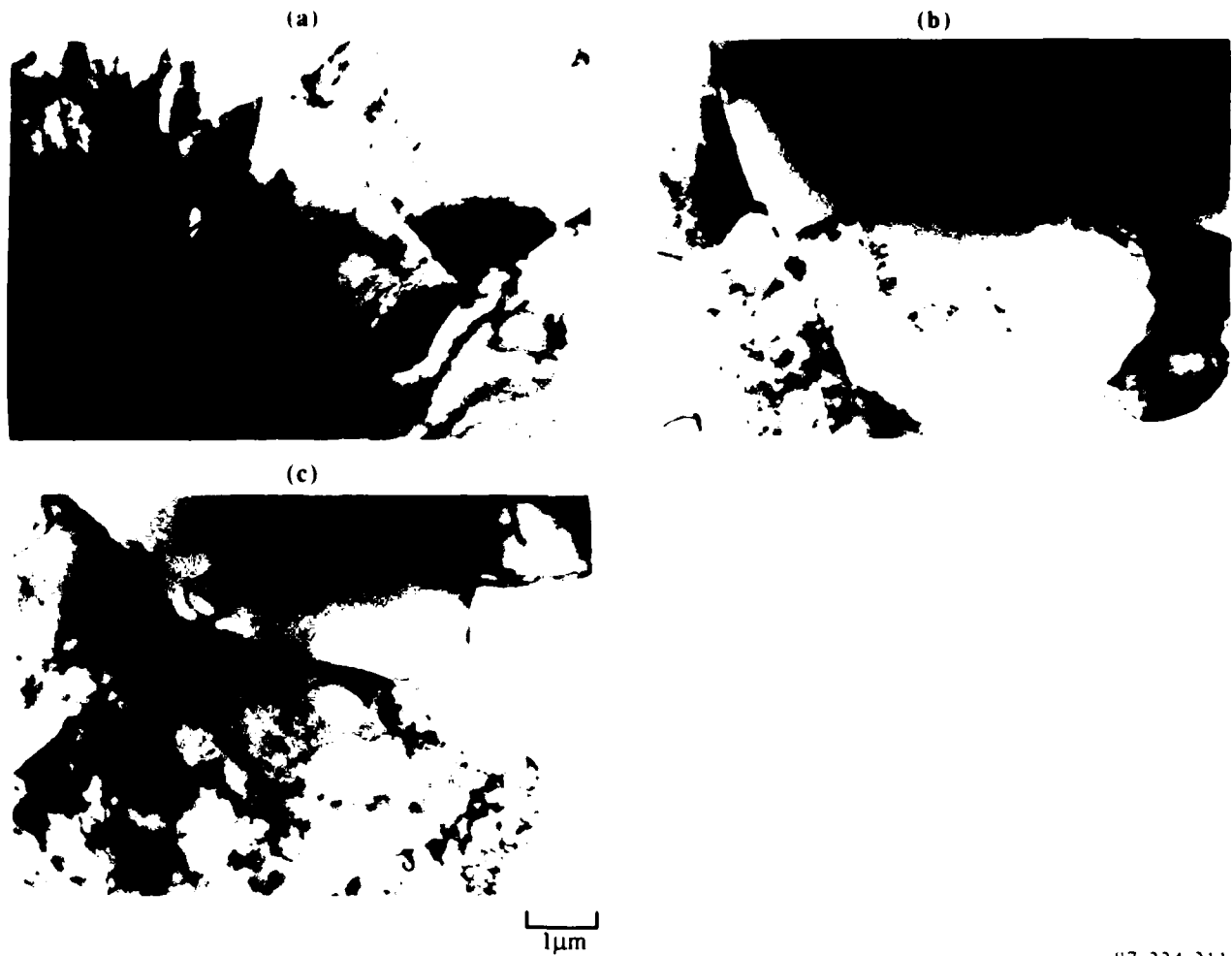
outgassing have a large volume fraction of coarse particles--probably oxides or hydroxides.

The microstructures of Al-Fe-Ce alloys shown in Figures 36 and 37 indicate that extrusions of these alloys must be done at $\approx 400^\circ\text{C}$ to prevent coarsening of dispersoids and to take advantage of fine dispersoids for high temperature creep resistance.



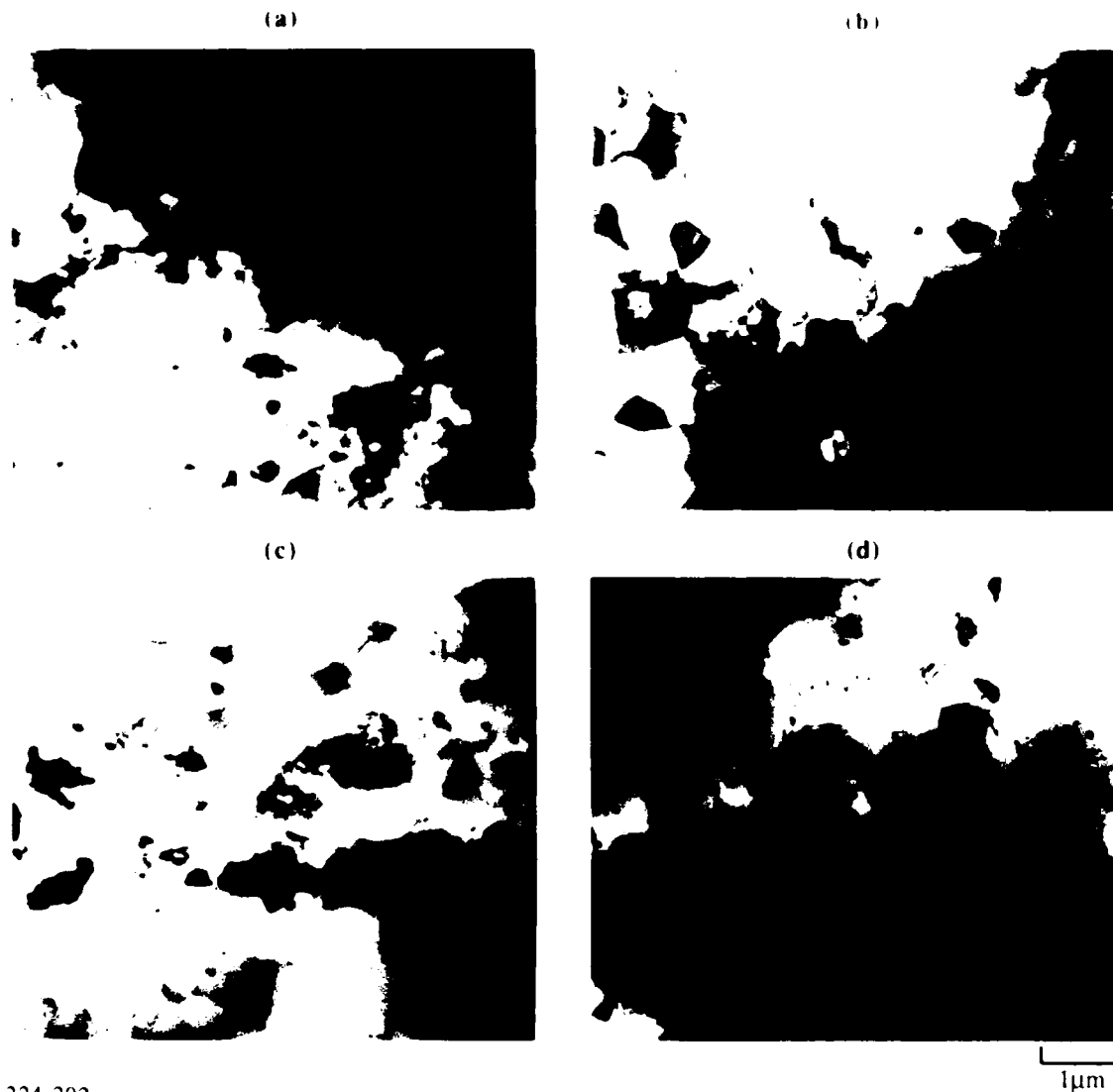
87-224-201

Figure 27. Transmission electron micrographs of 99.99% Al powders extruded at 400°C with an area reduction ratio of 16:1. (a,b) vacuum outgassed at 500°C , (c,d) without vacuum outgassing; (a,c) strain rate of 1.59/s, (b,d) strain rate of 0.23/s.



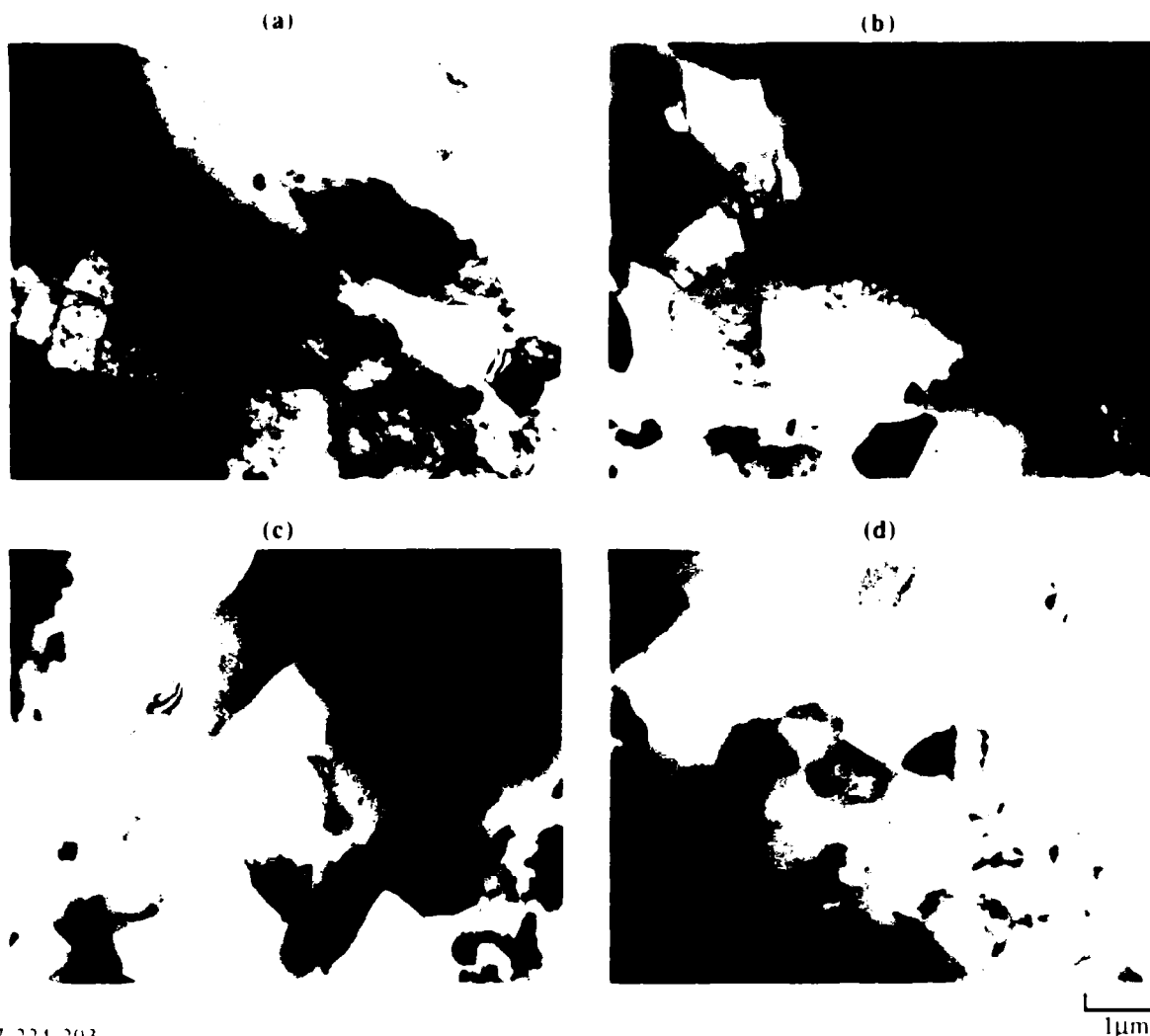
87-224-211

Figure 28. Transmission electron micrographs of 99.99% Al powders extruded at 450°C with an area reduction of 16:1. (a,b) without vacuum outgassing, (c) vacuum outgassed at 500°C; (a,c) strain rate of 1.59/s, (b) strain rate of 0.23/s.



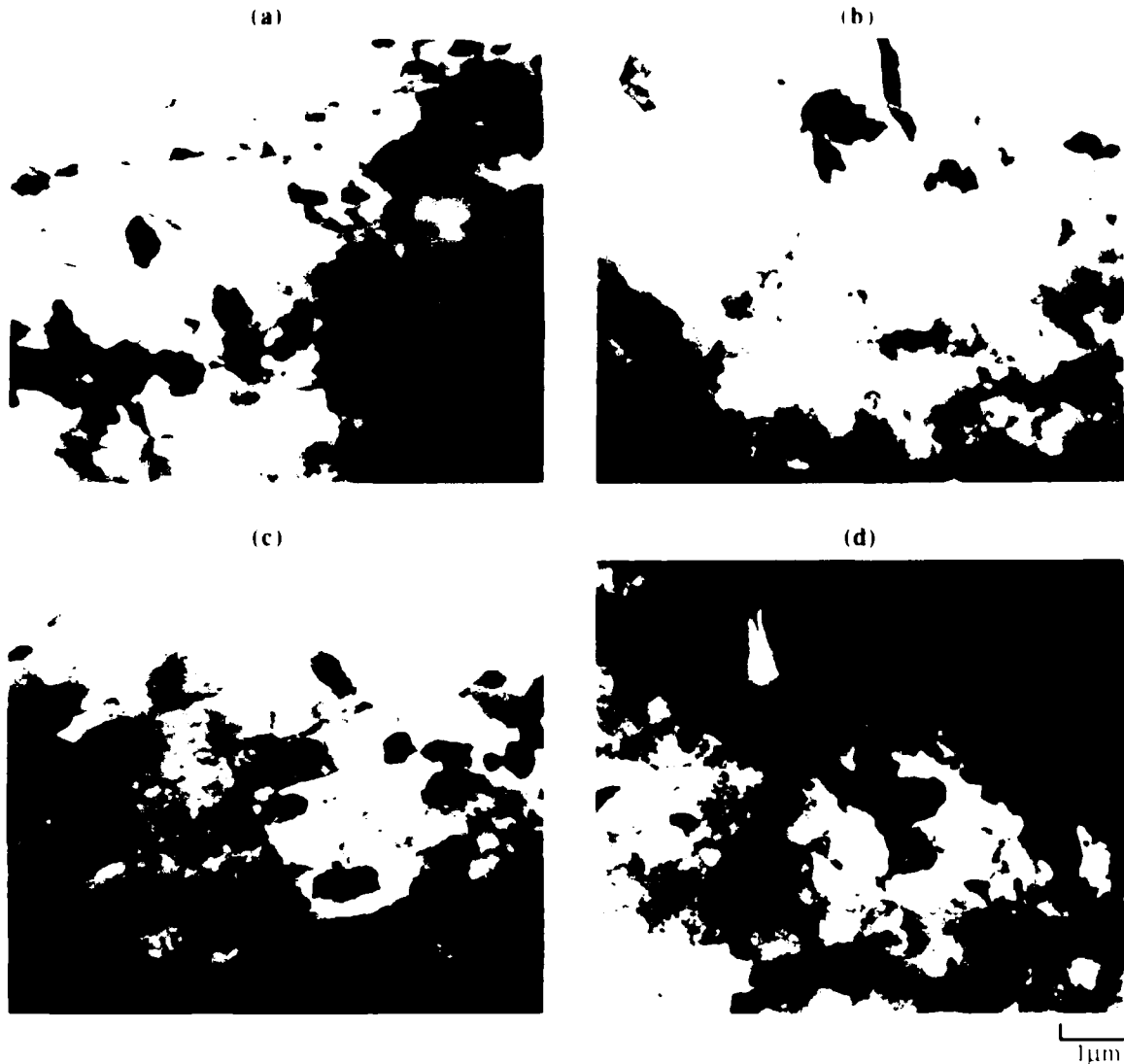
87-224-202

Figure 29. Transmission electron micrographs of Al-3Li-1Cu-1Mg-0.2Zr alloy powders vacuum outgassed at 500°C and extruded at 350°C with an area reduction ratio of 16:1. (a,b) strain rate of 1.59/s, (c,d) strain rate of 0.23/s; (a,c) longitudinal section, (b,d) transverse section.



87 224 203

Figure 30. Transmission electron micrographs of Al-3Li-1Cu-1Mg-0.2Zr alloy powders vacuum outgassed at 500 °C and extruded at 400 °C with an area reduction ratio of 16:1. (a,b) strain rate of 1.59/s, (c,d) strain rate of 0.23/s; (a,c) longitudinal section (b,d) transverse section.



87 224 205

Figure 31. Transmission electron micrographs of Al-3Li-1Cu-1Mg-0.2Zr alloy powders extruded at 350°C (without vacuum outgassing) with an area reduction ratio of 16:1. (a,b) strain rate of 1.59/s, (c,d) strain rate of 0.23/s; (a,c) longitudinal section, (b,d) transverse section.

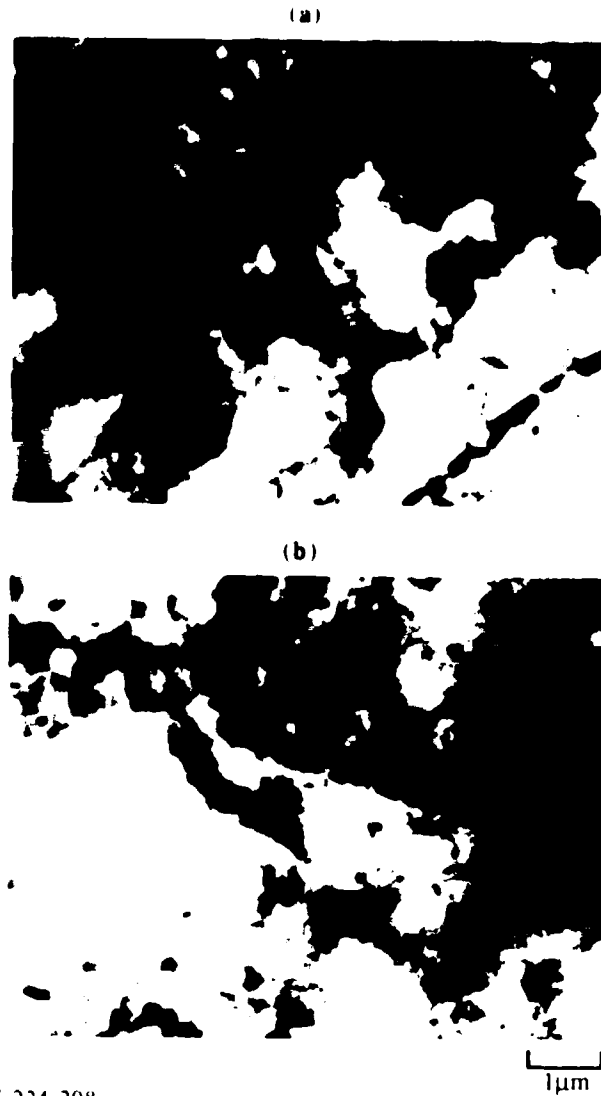
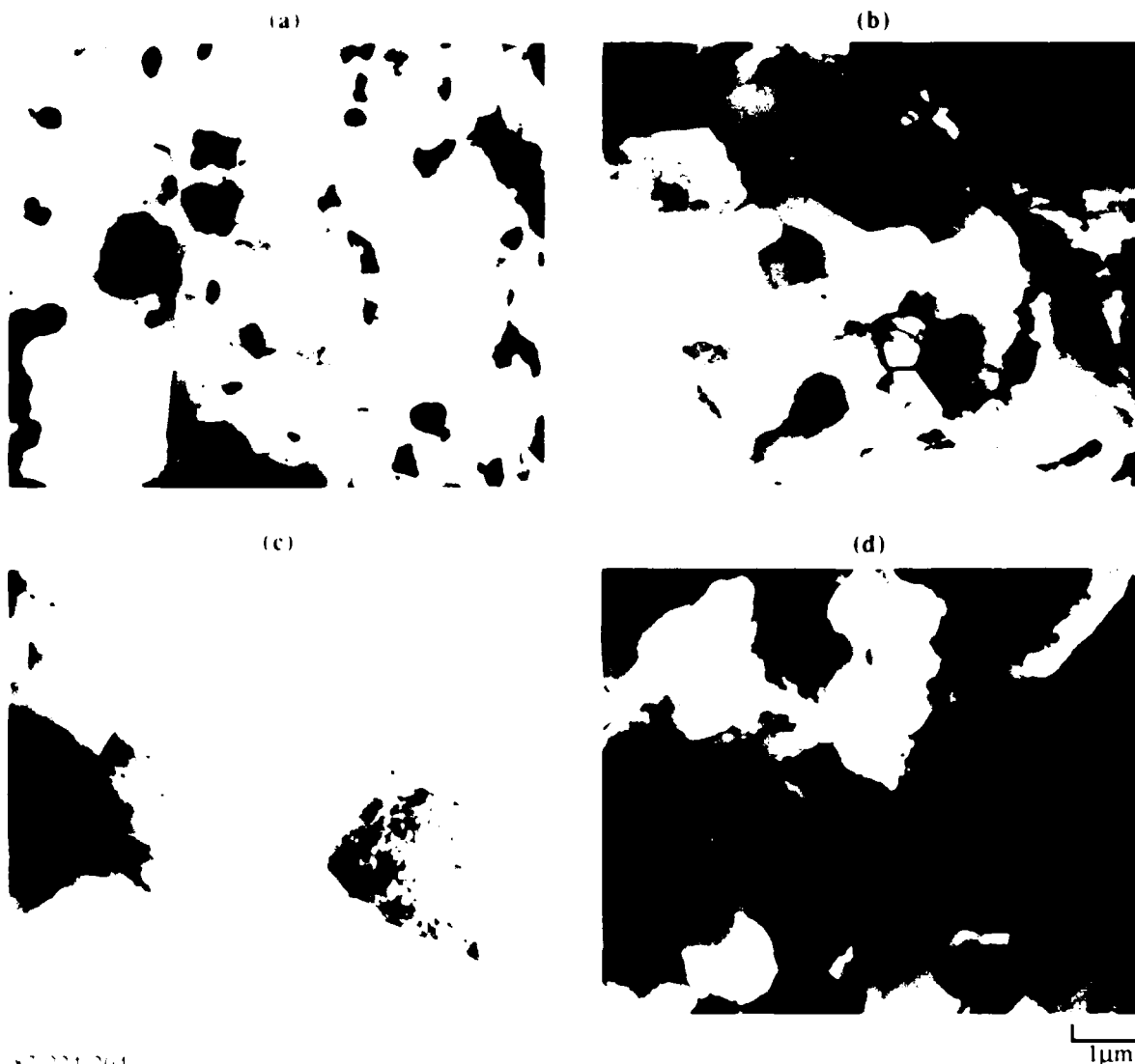
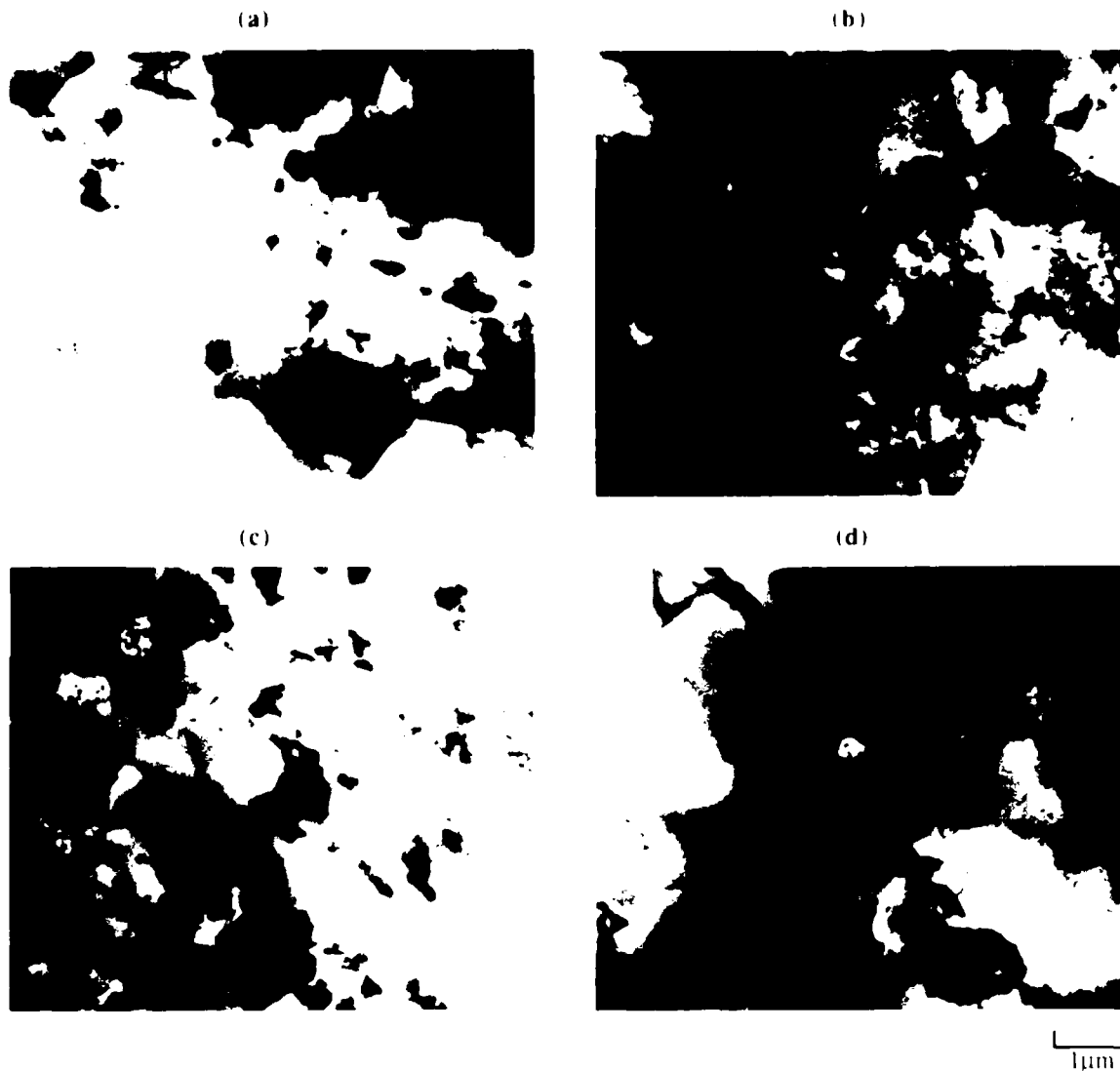


Figure 32. Transmission electron micrographs of Al-3Li-1Cu-1Mg-0.2Zr alloy powders extruded at 400°C (without vacuum outgassing) with an area reduction of 9:1 and strain rate of 1.59/s, (a) longitudinal section, and (b) transverse section.



87-224-204

Figure 33. Transmission electron micrographs of Al-3Li-1Cu-1Mg-0.2Zr alloy vacuum outgassed at 500°C and extruded at 430°C with an area reduction ratio of 16:1. (a,b) strain rate of 1.59/s, (c,d) strain rate of 0.23/s; (a,c) longitudinal section, (b,d) transverse section.



87-224-206

Figure 34. Transmission electron micrographs of Al-3Li-1Cu-1Mg-0.2Zr alloy powders extruded at 400 C (without vacuum outgassing) with an area reduction ratio of 16:1. (a,b) strain rate of 1.59/s, (c,d) strain rate of 0.23/s; (a,c) longitudinal section, (b,d) transverse section.

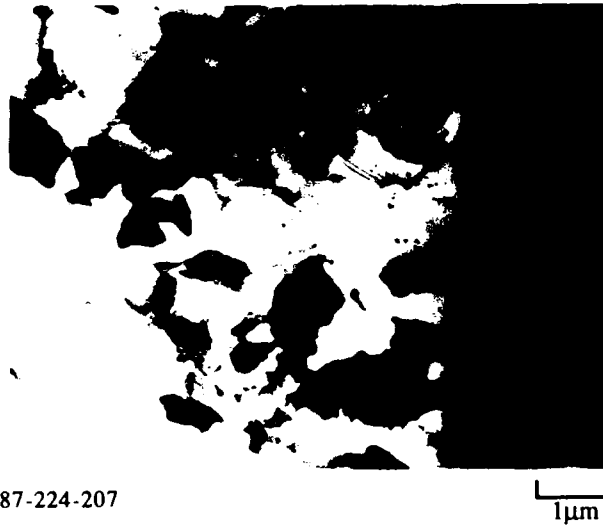
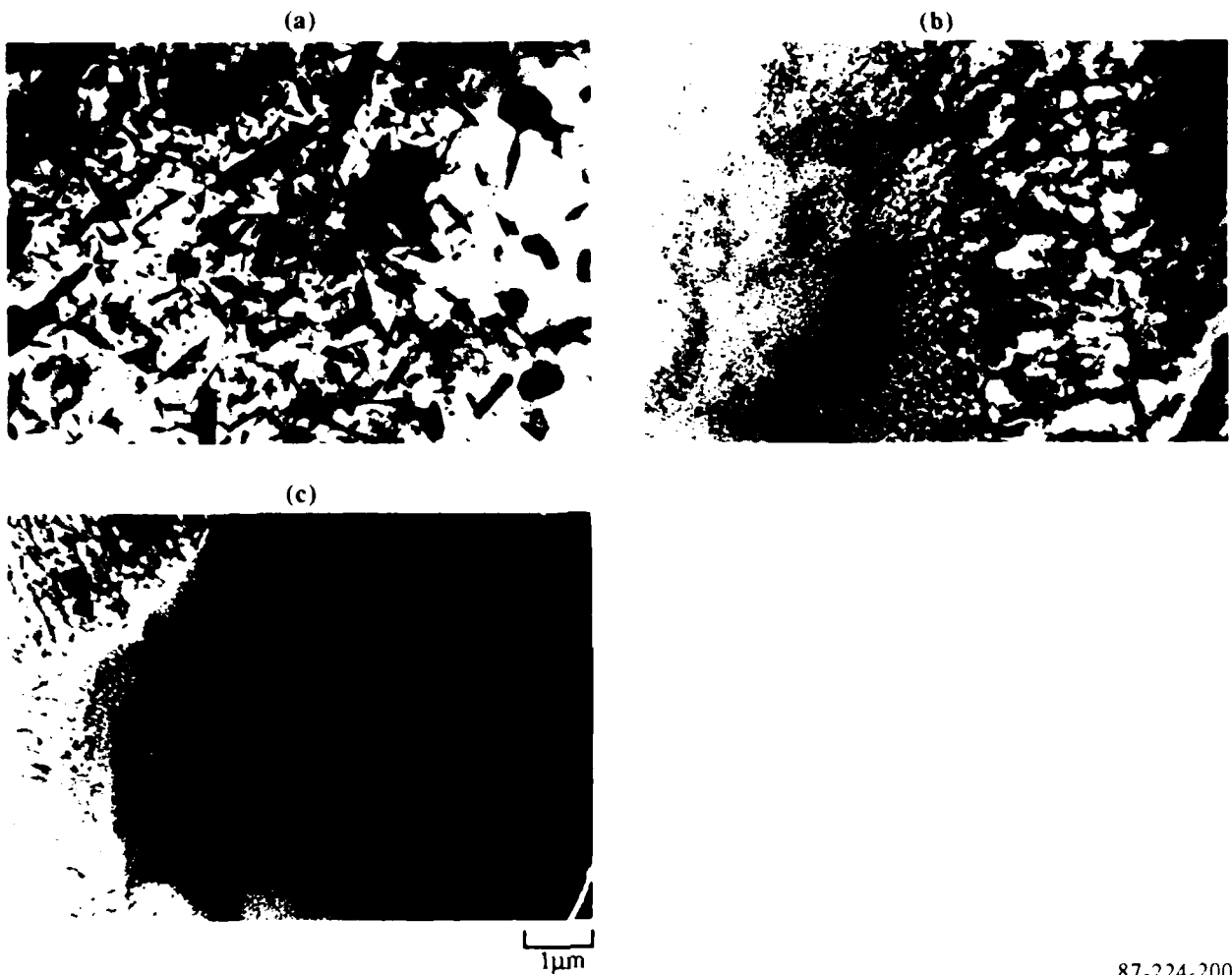
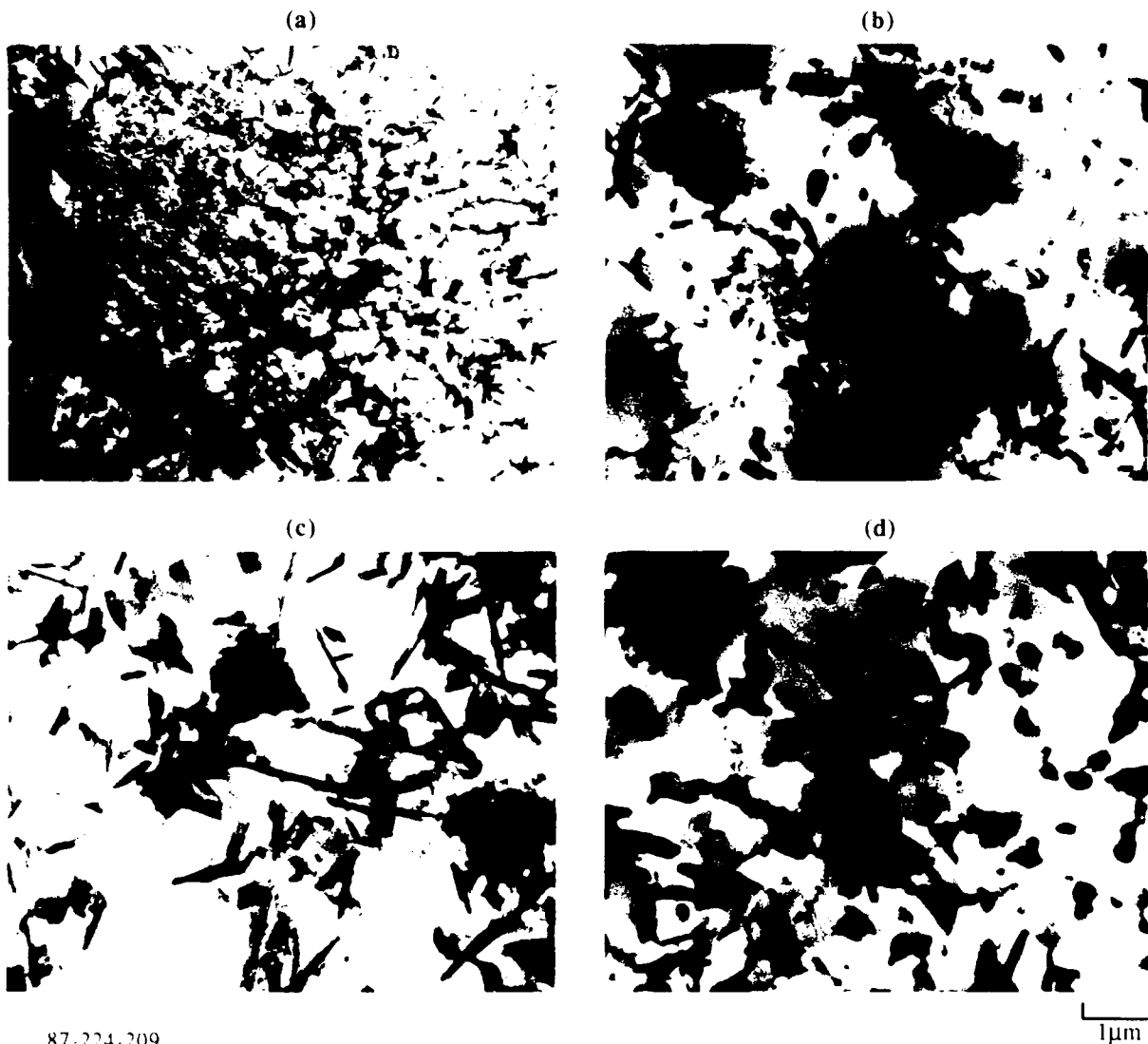


Figure 35. Transmission electron micrograph of Al-3Li-1Cu-1Mg-0.2Zr alloy powders extruded at 430°C (without vacuum outgassing) with an area reduction of 16:1 and strain rate of 1.59/s, longitudinal section.



87-224-200

Figure 36. Transmission electron micrographs of Al-8Fe-4Ce alloy powders; (a) as rapidly solidified, (b) annealed at 400°C for 2h, and (c) annealed at 500°C for 2h.



87-224-209

Figure 37. Transmission electron micrographs of Al-8.7Fe-7Ce alloy powders; (a,b) as rapidly solidified, (c) annealed at 400°C for 2, and (d) annealed at 500°C for 2.

4.4 Production Size Extrusions

Larger size billets were extruded at Nuclear Metals Inc., Concord, MA, at different temperatures, reduction ratios, geometries, and strain rates. Powders of 99.99% Al, Al-3Li-1Cu-1Mg-0.2Zr, and Al-8.0Fe-7Ce alloys were divided into seven lots each weighing 1.9 to 3.5 kg (4.1 to 7.8 pounds). These twenty-one lots were cold compacted at 230 kN (50 000 psi) in 88.9 mm (3.5 in.) O.D. by 85.7 mm (3.375 in.) 6061-T6 aluminum cans.

The cans were evacuated to 0.013 Pa; they were then heated while being pumped until the pressure decreased to 0.0013 Pa. The 14 billets of unalloyed aluminum and Al-3Li-1Cu-1Mg-0.2Zr were evacuated at $500 \pm 15^\circ\text{C}$. The 7 billets of the Al-8Fe-7Ce alloy were evacuated at $400 \pm 0/-15^\circ\text{C}$ to avoid the phase transition at 442°C . The canned compacts were heated to the desired extrusion temperature and held for a minimum of 2.25 hours prior to extrusion. Extrusions were performed using a 90.0-mm (3.545 in.) liner at 400°C in a 12.4-kN (1400 ton) press. Each billet was extruded at 2 or 3 different ram speeds for carefully determined intervals.

Materials at the nose and tail sections, and near the speed-change regions were discarded. Tensile specimens were machined from the unalloyed aluminum extrusions. Both tensile and fracture toughness specimens were machined from the Al-Li and the Al-Fe-Ce alloys.

4.5 Explosive Compaction of Aluminum Alloys

Under the currently employed static-consolidation conditions (high temperatures and pressures for several hours), certain amounts of recrystallization, grain growth, phase change, precipitation, and segregation are inevitable. Many of these microstructural changes diminish the effectiveness of heat treatments in controlling mechanical properties after consolidation. The ever-present surface oxide on individual Al-alloy particles is not easily broken and dispersed in the static-consolidation process, with the result that interparticle bonding is poor. Recently, explosive consolidation of Al alloys has been studied with the specific objectives of optimizing process parameters.^{9,10} In the present study the effects of material variables on densification and interparticle bonding during explosive consolidation were investigated. 99.9% Al, Al-3Li-1Cu-1Mg-0.2Zr, and Al-8Fe-7Ce alloys were selected for the study because of their large differences in hardness, flow stress, and work-hardening rate.

A schematic of the explosive compaction arrangement is shown in Figure 38. Compaction begins as the shock wave from a burning explosive travels through the top-end plug of the container into the metal powder pack. The compacting pressure generated by the shock wave violently agitates and compresses the individual powder particles in the pack. Large amounts of energy released by the chemical reactions in the explosive produce an instantaneous peak pressure which immediately readjusts itself to a more stable value at the Chapman-Jouquet (C-J) point, where all chemical reactions cease (Figure 38). Behind the C-J point, pressure dissipates relatively slowly through the expansion of the product gas. While the pressure dissipation is occurring, an inward pressure is exerted on the powder column. Depending on the type of explosive, a high-pressure pulse (several GPa) can be created. The pressure at the C-J point, P_{C-J} , may be estimated based on one-dimensional shock theory^{11,12} by

$$P_{C-J} = \frac{\rho_e V^2}{\gamma + 1}, \quad (7)$$

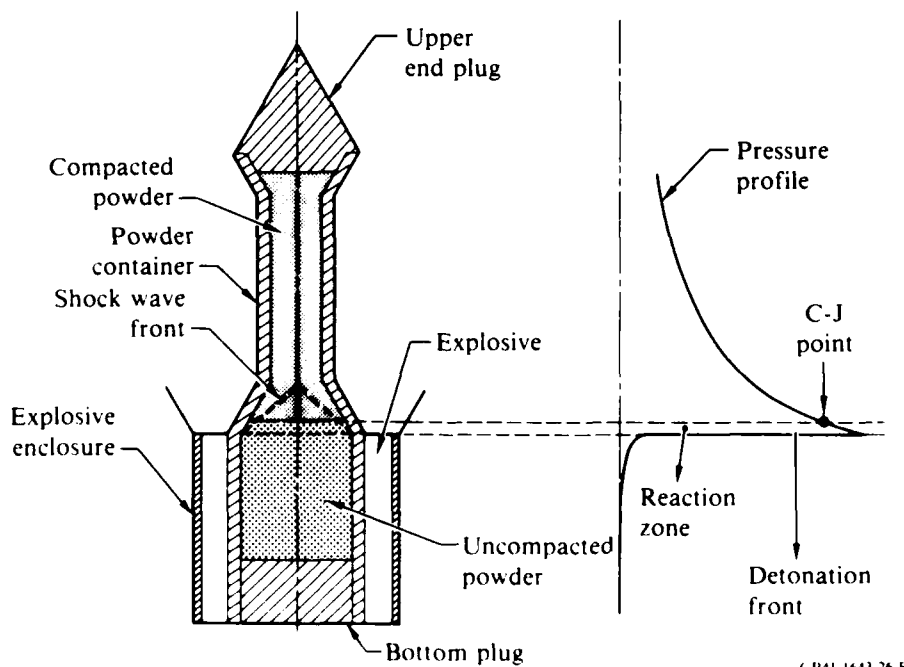


Figure 38. High-energy-rate consolidation of rapid solidification processed (RSP) alloys.

where ρ_e = density of the explosive powder, γ = specific heat ratio of the product gas, and V = detonation velocity. The detonation velocity V is related to the heat, Q , released from the explosives by

$$V^2 = 2Q(\gamma^2 - 1) . \quad (8)$$

V and Q can be measured experimentally; γ can thus be determined and the compaction pressure P_{C-J} calculated. Values of P_{C-J} for most explosives ranges from 1 to 60 GPa. The compaction pressures can be varied by varying the explosives. The high energy density behind the shock can melt the particle surface layers to form strong interparticle bonds and leave the bulk microstructure unaltered. When the shock wave reaches the lower end plug, the compacting pressure is further increased by the shock wave reflection.

Alloy powders were packed into 3.2-cm-diameter and 14-cm-long mild steel cylinders (Figure 39). The powder column was packed by repeated tapping followed by vibrating for 20 hours under vacuum and then cold-pressing to maximum packing density. The assembled powder pack was supported by the fly-plate and surrounded by the fly-tube with a 2-mm gap (Figure 40). The test arrangement provided an extended explosive column above the powder pack to insure the development of a plane detonation front traveling longitudinally downward. The tests were performed underground, and the underground wall

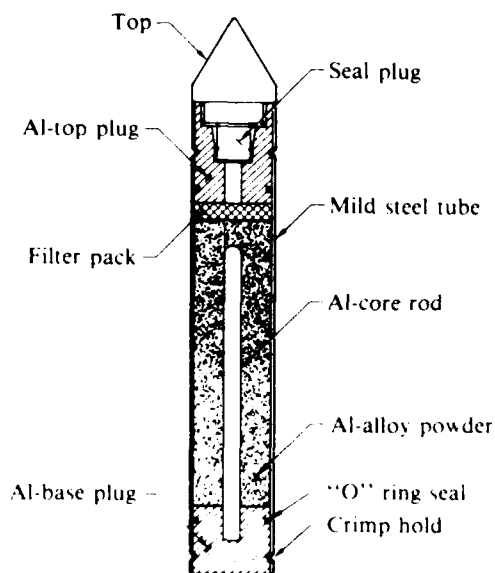


Figure 39. Powder pack as assembled.

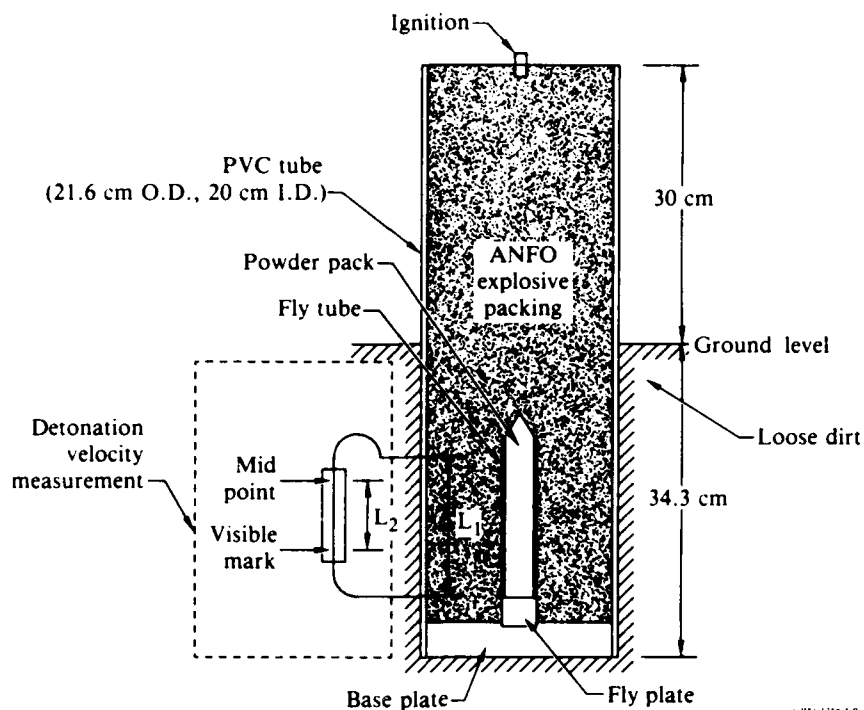


Figure 40. Test arrangement for explosive compaction with detonation velocity measurement.

helped to contain the momentary explosive pressure during consolidation. The baseplate was used to reflect the detonation wave for further enhancement of the consolidation. Test parameters used in this study are listed in Table 6.

The explosive consolidation tests were conducted at the Center of Explosive and Technology Research (CETR), New Mexico Institute of Mining and Technology, Socorro, NM. For each test, the detonation velocity of the explosive was measured by the Dautriche method (Figure 40) in which the two ends of a length of primacord are inserted into the explosive a distance L_1 apart. The burning explosive ignites the primacord ends as it reaches them in turn, and the primacord burns towards the center from each end. The point on the primacord where the ignition from the two ends meet leaves a visible mark. The detonation velocity is given by

$$V_D = \frac{V_a L_1}{2L_2} \quad (9)$$

Table 6. Test parameters and consolidate properties for explosive compactions (3590m/s measured detonation speed and 3.7 GPa estimated peak)

Test No.	Powder used	Al-core diam (mm)	Packing density (%T.D.*)	Comsolidate Properties		
				Density (%T.D.)	Tensile strength (MPa)	Tensile strength of extruded samples (MPa)
1	99.9%	6.4	52	100	74.5	100 [15]
2	Al-3Li-1Cu-1Mg-0.2Zr	6.4	65	97.6	207	
3	Al-8.4Fe-7Ce	6.4	67	99	256	287**

* T.D.=Theoretical density

** Measured values

87-224-212

where V_{α} = the known detonation velocity of the primacord,

L_1 = the distance between the two primacord inserts in the explosive container, and

L_2 = the measured distance between the visible test mark and the midpoint of the primacord.

The tests were designed to produce a peak pressure of 3.7 GPa generated immediately behind a detonation front traveling at $3590 \text{ m}\cdot\text{s}^{-1}$ and attenuated by a rarefaction wave following the detonation front (Figure 41). The initial peak pressure pushes the fly-tube onto the powder pack with a large momentum, generating a compression wave in the packed powder column. However, the peak pressure of this compression wave in the powder column is less than 3.7 GPa because of the energy loss in deforming both the fly- and powder-tubes. The duration of the peak pressure in the powder is considerably longer than in the detonation wave because of the inward momentum of the collapsing fly- and powder-tubes.

The pressure profiles and wave patterns during compaction are illustrated in Figure 41. The primary compression wave (C) reflected from the core rod at the center of the powder pack generates a reflected compression wave (RC) with a peak pressure several times that of the primary compression wave. The combined primary and secondary compression waves generate high energy pulses at the powder particle boundaries resulting in temperature spikes, disintegration of oxide film, and local melting, all of which contribute to the densification and interparticle bonding within the explosive compacts. The rarefaction

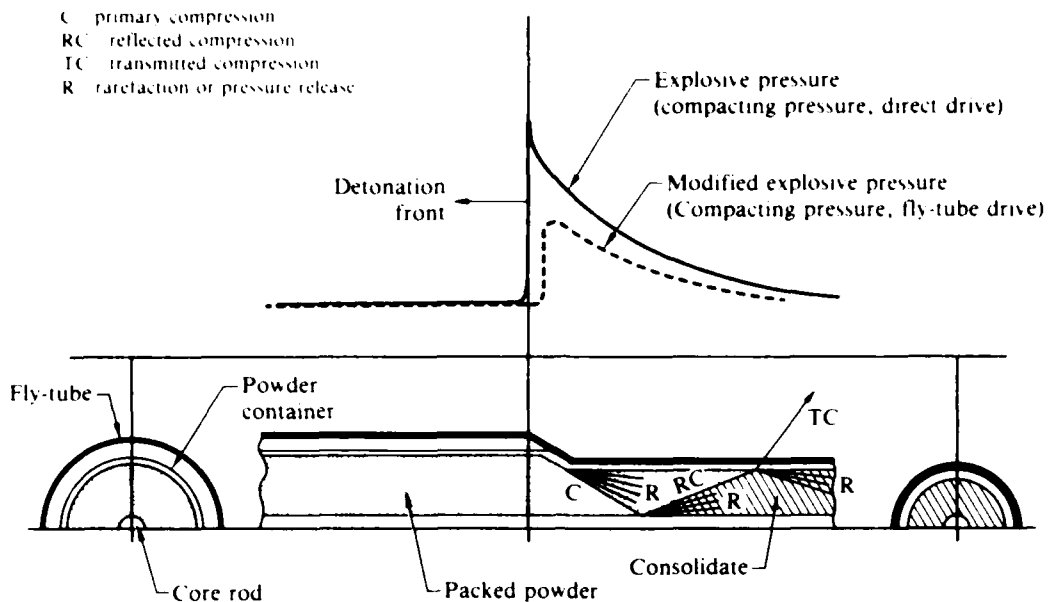


Figure 41. Pressure profiles and wave patterns during explosive compactions.

waves behind each compression wave can, under certain conditions produce tensile stresses and cracks between the compacted particles and layers. Hence, a precise control of the intensity and duration of the rarefaction waves is necessary to minimize cracks in the explosive compacts.

The fly-tube approach employed in this study has been successful in producing crack-free explosive compacts. The parameters which contribute to improved consolidation are material and size of the fly-tube, peak-pressure decay rate, and increased hold time of the compression in the powder medium effected by the momentum of the fly-tube.

The explosive compacts were sectioned in transverse and longitudinal directions for optical and electron-microscopic examinations. The microstructures of explosively consolidated samples are shown in Figures 42a-42c, and fracture surfaces are shown in Figures 43 and 44.

Representative samples were cut from the compacts for density measurements by the neutral buoyancy method and for tensile strength measurements. Tensile properties were measured on 10.0 × 3.0 × 2.5 mm specimens.

Optical micrographs of explosively consolidated specimens shown in Figures 42a-42c indicate significant particle-surface melting and good interparticle

bonding in all the alloys. The tensile fracture surfaces of the specimens, shown in Figures 43 and 44 indicate transparticle fracture in all the specimens, again indicative of sound interparticle bonding. Densification and interparticle bonding during explosive consolidation are not influenced by minor changes in material properties.

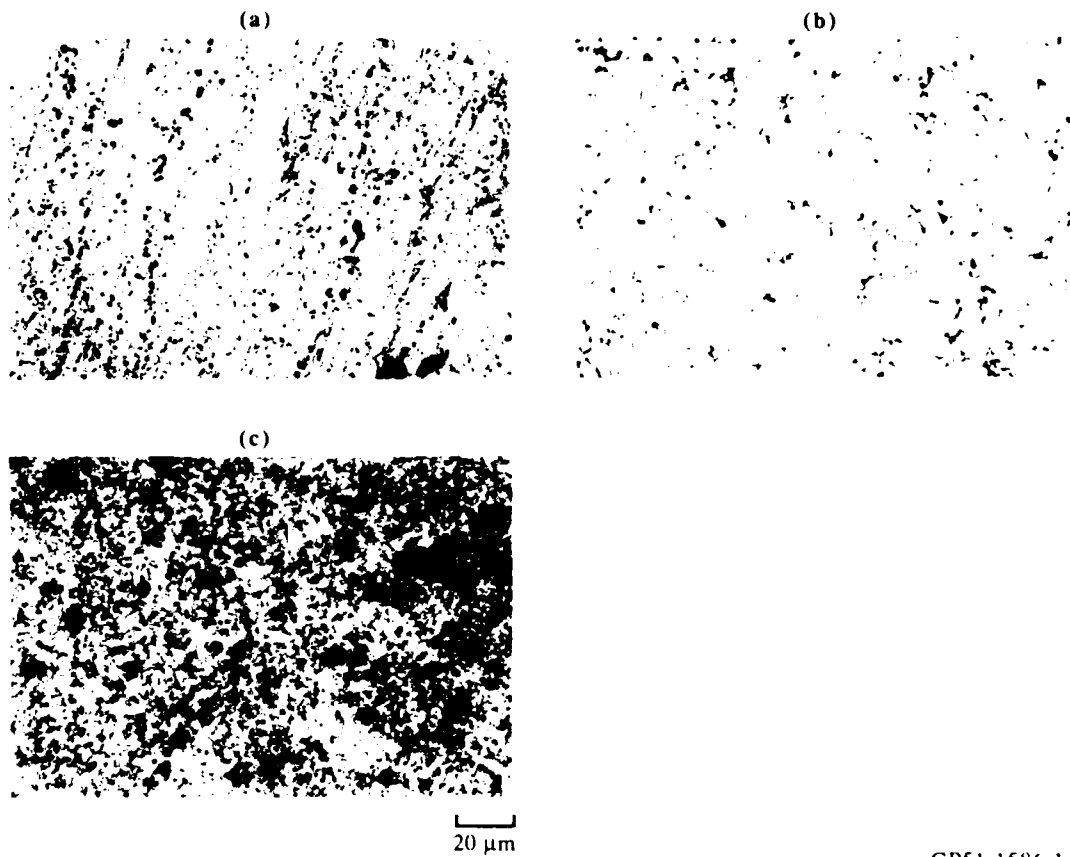
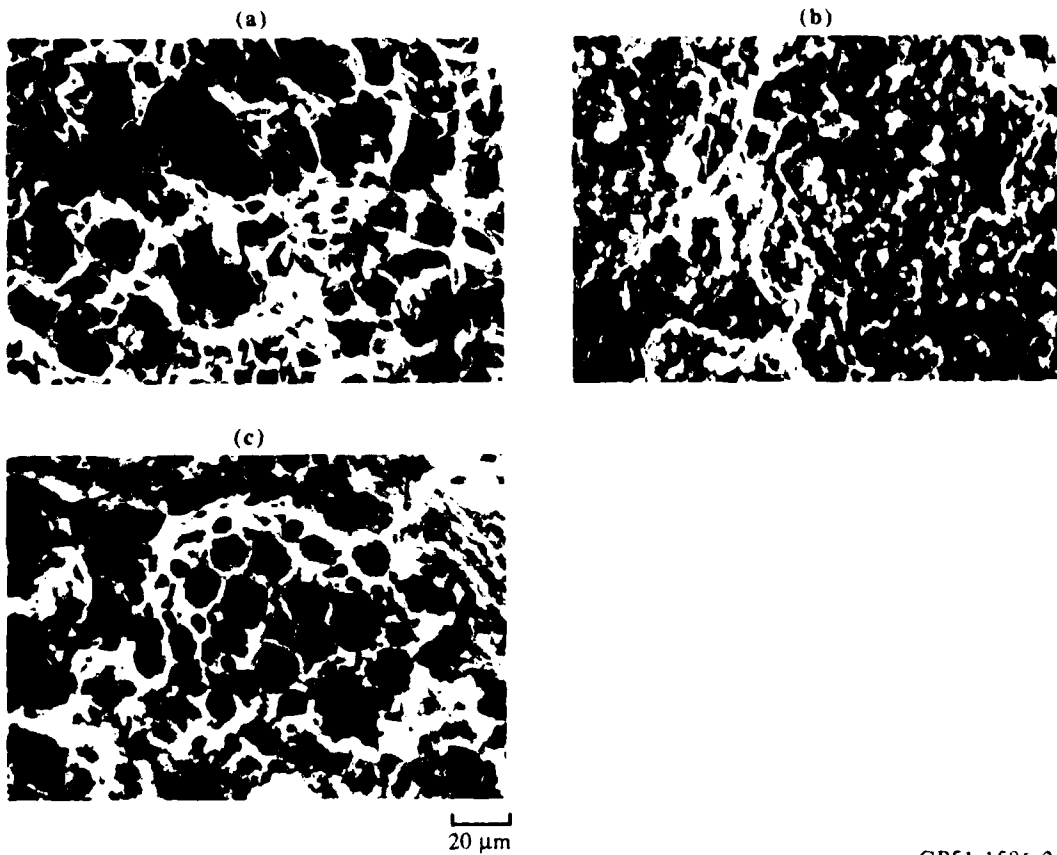
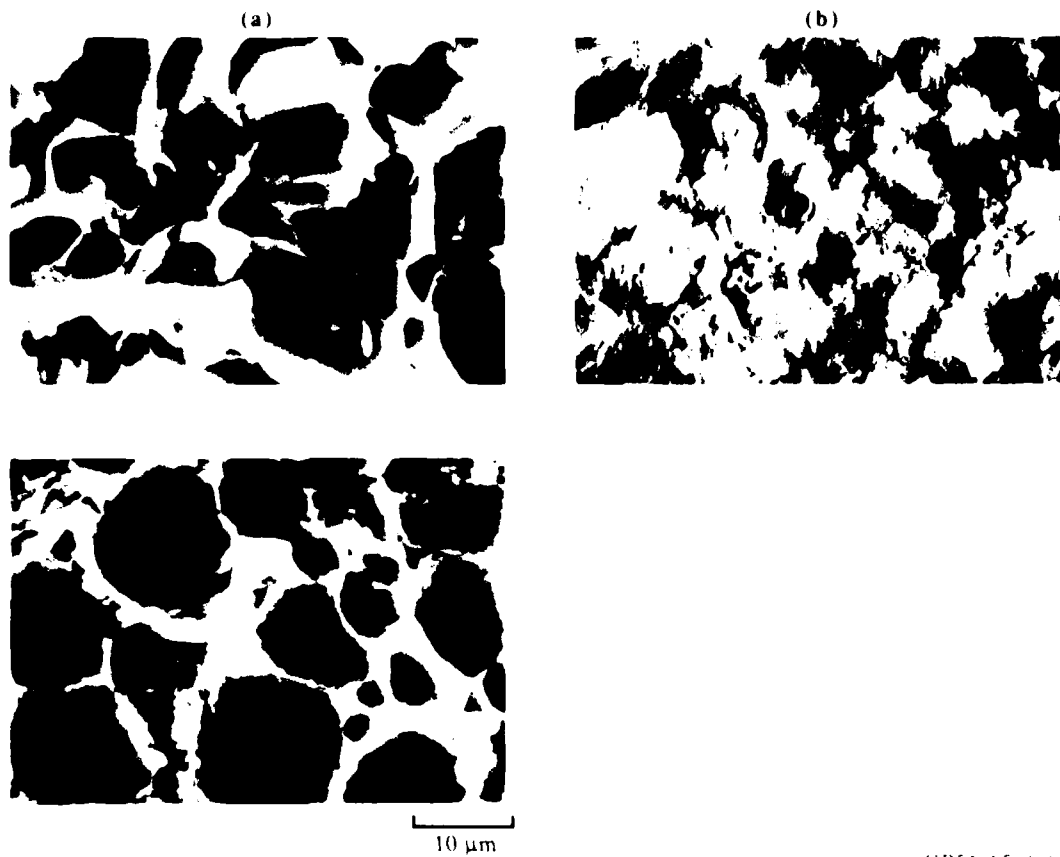


Figure 42. Optical micrographs of explosive compacts of (a) 99.9% Al, (b) Al-3Li-1Cu-1Mg-0.2Zr, and (c) Al-8.4Fe-7Ce alloys.



GP51-1586-2-R

Figure 43. Scanning electron micrographs of tensile fracture of explosive consolidated (a) 99.9% Al, (b) Al-3Li-1Cu-1Mg-0.2Zr, and (c) Al-8.4Fe-7Ce alloys.



GP51 1586 6 R

Figure 44. Scanning electron micrographs of tensile fractures of explosively consolidated (a) 99.9% Al, (b) Al-3Li-1Cu-1Mg-0.2Zr, and (c) Al-8.4Fe-7Ce alloys.

5. CONSOLIDATION PROCESS, MICROSTRUCTURE, AND PROPERTY INTERRELATIONSHIP IN RAPIDLY SOLIDIFIED ALUMINUM ALLOYS

5.1 Flow Stress - Strain Rate Relationships

The flow-stress/strain-rate relationships for Al and Al-3Li-1Cu-1Mg-0.2Zr are shown in Figures 45 and 46, respectively. The low values of the strain rate sensitivity, m , indicate that the extrusion process is relatively insensitive to strain rate. For a given temperature, m is nearly constant at all strain rates.

5.2 Consolidation Process Modeling

Prasad et al.¹³ have developed a method of modeling dynamic material behavior in which the dissipated power is partitioned between dynamic metallurgical processes and viscoplastic heat components. The dynamic metallurgical process co-content J is related to the deformation parameters by

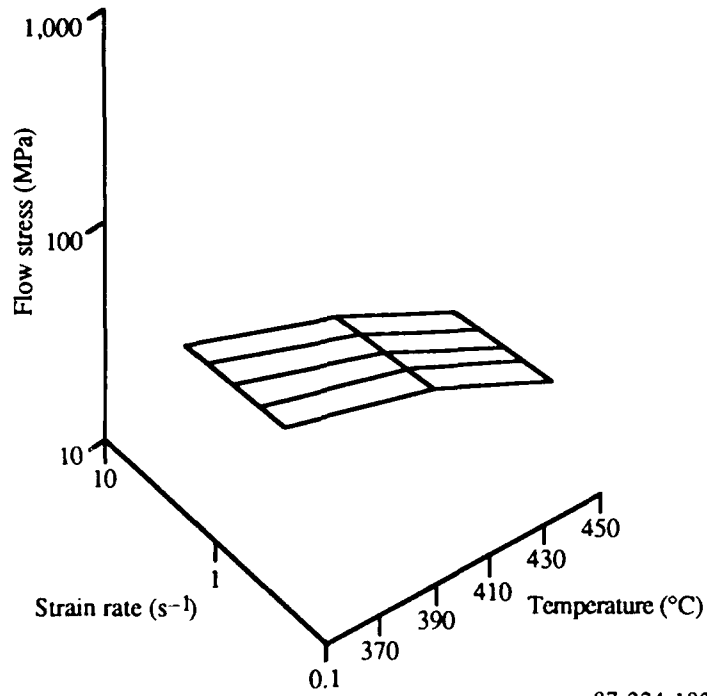
$$J = \frac{\sigma \dot{\epsilon}^m}{m + 1} \quad (10)$$

where σ is the flow stress, $\dot{\epsilon}$ is the strain rate, and m is the strain rate sensitivity. The efficiency of dissipation, η , which is the ratio of J to the maximum possible value of J is given by

$$\eta = 2m/(m+1) \quad (11)$$

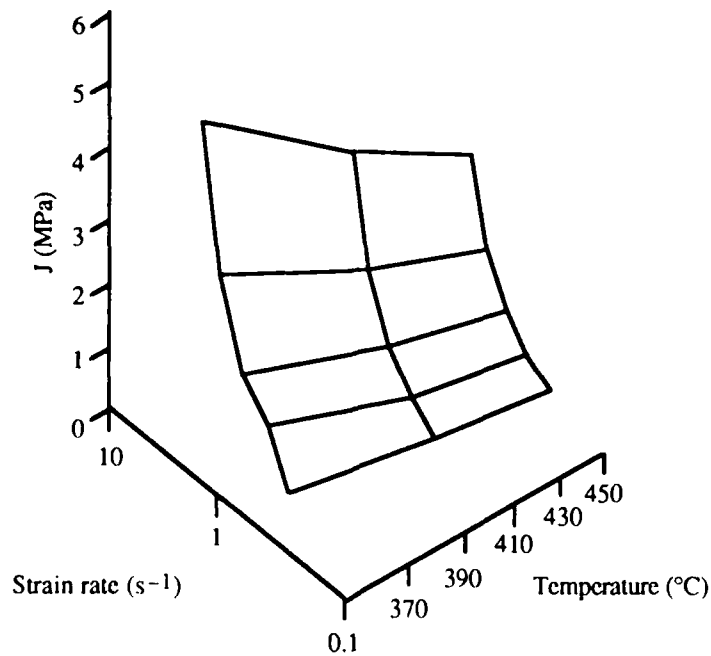
The optimum temperature and strain-rate conditions are those corresponding to peaks in the J co-content and efficiency of dissipation without causing internal fractures. The J co-content for Al is plotted as a function of strain rate and temperature in Figure 47. The J co-content increases with increasing strain rate and is relatively temperature insensitive. Hence, the optimum extrusion conditions are predicted to be at faster strain rates at lower temperatures.

The J co-content for Al-3Li-1Cu-1Mg-0.2Zr alloy increases with temperature as well as strain rate as shown in Figure 48. Hence, extrusions should be performed as fast as possible at the highest temperature.



87-224-182

Figure 45. Effect of extrusion temperature and strain rate on extrusion flow stress for unalloyed Al.



87-224-184

Figure 46. Effect of isothermal extrusion temperature and strain rate on co-content J of unalloyed aluminum.

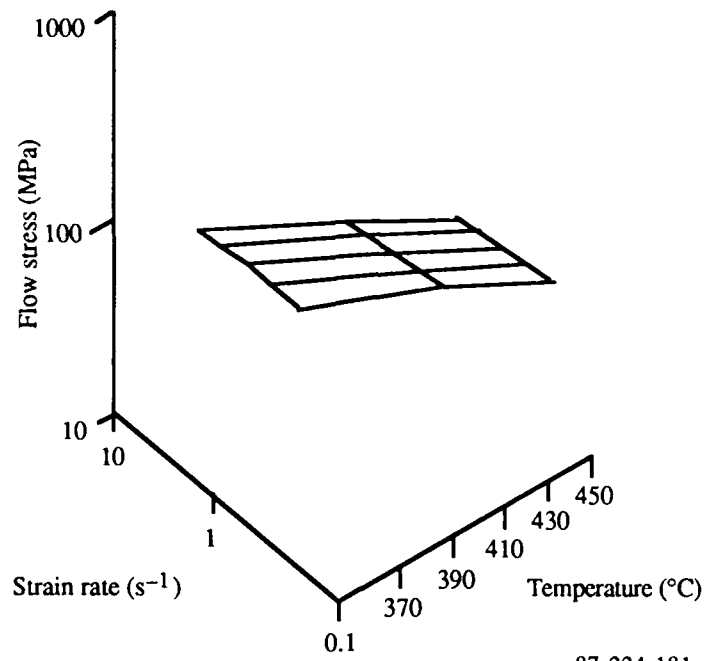


Figure 47. Effect of extrusion temperature and strain rate on extrusion flow stress for Al-3Li-1Cu-1Mg-0.2Zr.

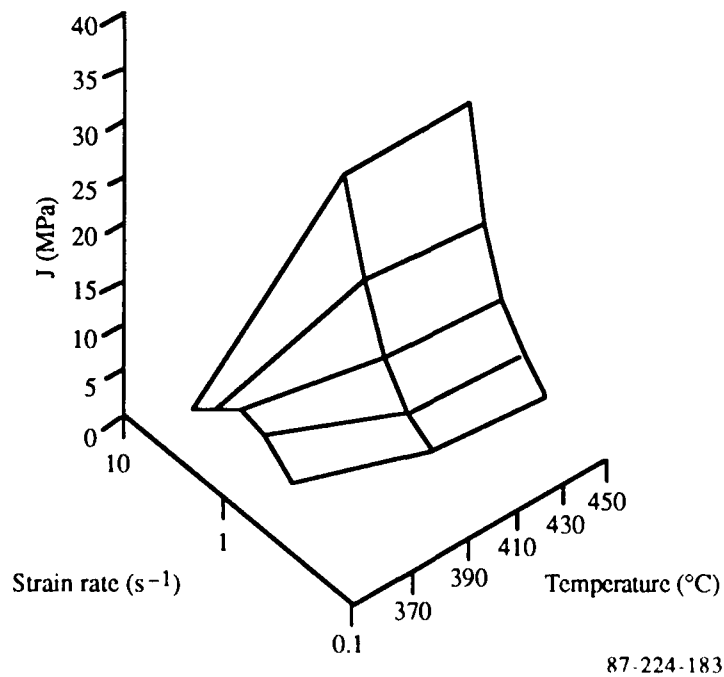


Figure 48. Effect of isothermal extrusion temperature and strain rate on co-content J of Al-3Li-1Cu-1Mg-0.2Zr.

5.3 Interrelationship Between Consolidation Process and Product Mechanical Properties

5.3.1 Properties of Isothermal Extrusions

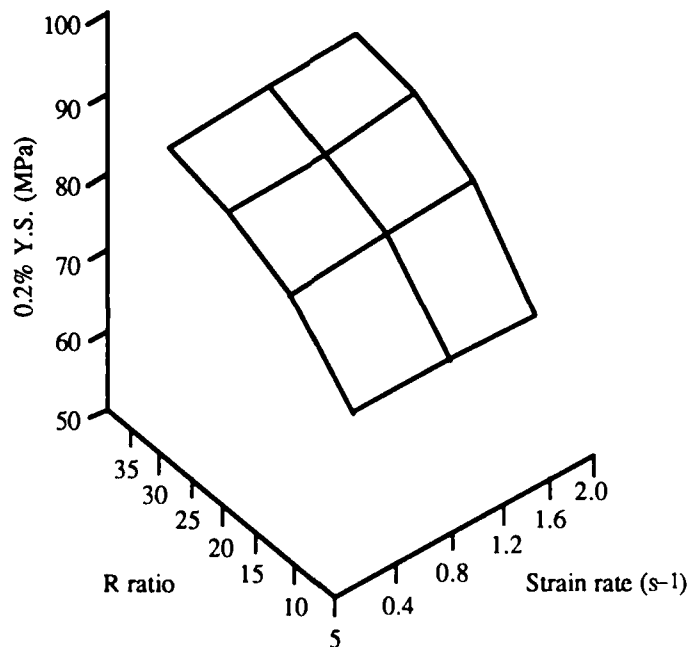
The interrelationships between yield stress and extrusion parameters are shown in Figures 49 and 50 for 99.99% Al. For Al, the yield stress is a weak function of temperature and strain rate. Yield stress increases with increasing reduction ratio (R).

For the Al-3Li-1Cu-1Mg-0.2Zr alloy, the yield stress is higher in specimens extruded at higher strain rates and higher temperatures (Figures 51 and 52).

Extrusion ratio has no significant effect on properties of the alloys.

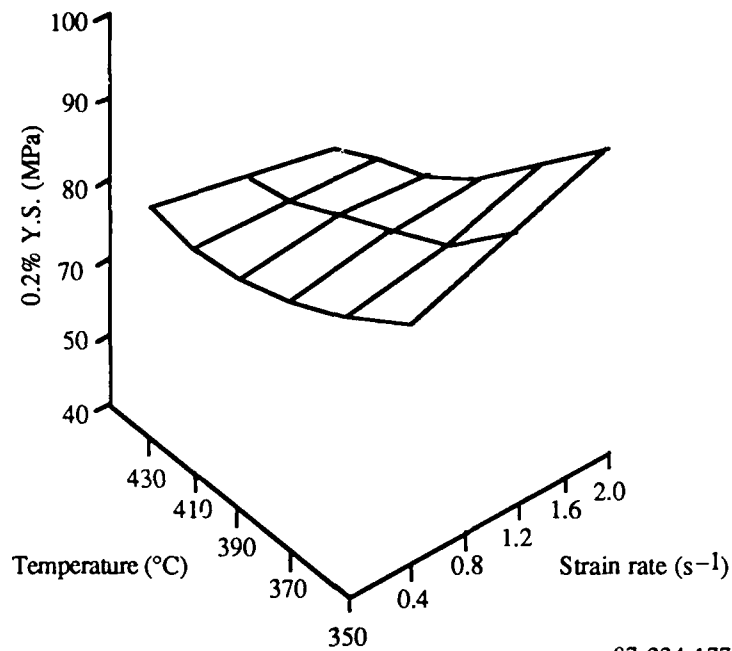
5.3.2 Properties of Production Size Extrusions

The extrusions produced at Nuclear Metals, Inc., were evaluated for yield stress, ultimate tensile strength, elongation, and fracture toughness. The results are summarized in Tables 7-10. The properties of solution treated and aged Al-3Li-1Mg-1Cu-0.2Zr shown in Table 8 indicate the best combination of



87-224-180

Figure 49. Effect of extrusion ratio (R) and strain rate on the room temperature yield stress of unalloyed aluminum isothermally extruded at 400°C.



87-224-177

Figure 50. Effect of extrusion temperature and strain rate on the room temperature yield stress of unalloyed aluminum isothermally extruded at a ratio of 16:1.

yield stress, ultimate tensile strengths, ductility, and fracture toughness are produced by extruding the alloy at 400°C, a strain rate of 0.86 s⁻¹, and a reduction ratio of 16:1. 559 MPa ultimate tensile strength, 5.4% elongation, and 36.6 MPa \sqrt{m} fracture toughness (Table 10) represent the best combination of properties that has ever been achieved in this class of alloys.

5.3.3 Properties of Explosively Consolidated Compacts

Densities of the explosive consolidates of this study varied between 97 and 100% of the theoretical densities of the alloys (Table 6). Tensile strengths of the consolidates ranged from 74.5 MPa for 99.9% Al to 282 MPa for the Al-3Li alloy (Table 6). These values which are 72-98% of the strengths of extruded samples, clearly indicate the suitability of the process for producing sound compacts. The strengths can be further improved by subsequent thermomechanical processing and heat treatment. The tensile strength of aluminum in the explosively consolidated condition approaches that in the extruded condition (Table 6).

Table 7. Effects of extrusion parameters on mechanical properties of unalloyed aluminum in as-extruded condition.

Extrusion parameters				Mechanical properties		
Temperature (°C)	R ratio	Aspect ratio	Strain rate (s ⁻¹)	0.2% Y.S. [MPa (ksi)]	U.T.S. [MPa (ksi)]	Elongation (%)
450	16	4.3	0.63	66.8(9.7)	100.6(14.6)	42.4
450	16	4.3	0.97	68.4(9.9)	100.4(14.6)	37.2
450	16	4.3	1.77	68.3(9.9)	100.6(14.6)	41.9
400	16	4.3	0.57	70.5(10.2)	104.8(15.2)	42.0
400	16	4.3	1.31	68.7(10.0)	102.6(14.9)	35.0
400	16	4.3	2.17	70.5(10.2)	102.4(14.9)	35.7
350	16	4.3	0.57	73.6(10.7)	101.5(14.7)	33.8
350	16	4.3	0.91	69.2(10.0)	100.2(14.5)	41.1
350	16	4.3	2.00	71.7(10.4)	100.5(14.6)	35.3
300	16	4.3	0.57	73.5(10.7)	102.4(14.9)	37.7
300	16	4.3	0.91	72.3(10.5)	101.6(14.7)	37.5
300	16	4.3	2.00	73.0(10.6)	102.7(14.9)	37.5
300	16	1.0	0.46	77.8(11.3)	102.4(14.9)	33.1
300	16	1.0	0.86	78.0(11.3)	100.6(14.6)	27.9
300	16	1.0	1.72	82.7(12.0)	102.7(14.9)	27.8
300	31	5.0	0.55	71.3(10.3)	99.5(14.4)	37.2
300	31	5.0	0.97	69.4(10.1)	100.7(14.6)	36.5
300	31	5.0	2.14	76.4(11.1)	103.6(15.0)	36.5
350	31	5.0	0.69	70.4(10.2)	100.6(14.6)	38.0
350	31	5.0	1.18	68.1(9.9)	99.7(14.5)	38.1

87-224-187

Table 8. Effect of extrusion parameters on mechanical properties of Al-3Li-1Mg-1Cu-0.2Zr after solution treatment and aging (560°C/1 h/WQ; 177°C/24 h/AC).

Extrusion parameters				Mechanical properties			
Temperature (°C)	R ratio	Aspect ratio	Strain rate (s ⁻¹)	0.2% Y.S. [MPa(ksi)]	U.T.S. [MPa(ksi)]	Elongation (%)	Fracture toughness [MPa√m (ksi√in.)]
500	16	4.3	0.57	467(67.7)	557(80.8)	4.4	21.4(19.5)
500	16	4.3	0.80	472(68.5)	564(81.8)	4.7	24.9(22.6)
500	16	4.3	1.66	455(66.0)	509(73.8)	3.1	—
450	16	4.3	0.57	—	—	—	20.1(18.3)
450	16	4.3	0.74	475(68.9)	538(78.0)	3.9	—
450	16	4.3	1.71	468(67.9)	532(77.2)	4.7	18.7(17.0)
400	16	4.3	0.57	466(67.6)	557(80.8)	5.4	—
400	16	4.3	0.91	459(66.6)	551(79.9)	4.6	—
400	16	4.3	1.83	458(66.4)	564(81.8)	5.7	21.6(19.6)
350	16	4.3	0.57	459(66.6)	543(78.8)	5.7	19.0(17.3)
350	16	4.3	0.86	454(65.8)	546(79.2)	5.7	20.2(18.4)
350	16	4.3	1.60	454(65.8)	546(79.2)	6.4	23.8(21.6)
400	16	1.0	0.57	525(76.1)	591(85.7)	4.6	29.1(26.5)
400	16	1.0	0.86	519(75.3)	559(81.1)	5.4	36.6(33.0)
400	16	1.0	1.72	516(86.1)	594(86.1)	2.8	29.2(26.5)
400	31	5.0	0.55	459(39.2)	552(80.1)	5.2	20.8(18.9)
400	31	5.0	0.80	461(66.9)	561(81.4)	5.3	20.1(18.3)
400	31	5.0	1.94	405(58.7)	455(66.0)	4.5	—
450	31	5.0	0.55	470(68.2)	571(82.8)	5.0	19.7(17.9)
450	31	5.0	1.73	486(70.5)	592(85.9)	6.2	—
450	31	5.0	2.63	461(66.9)	551(79.9)	4.8	22.9(20.8)

87-224-189

Table 9. Effect of extrusion parameters on mechanical properties of Al-8Fe-7Ce in as-extruded condition.

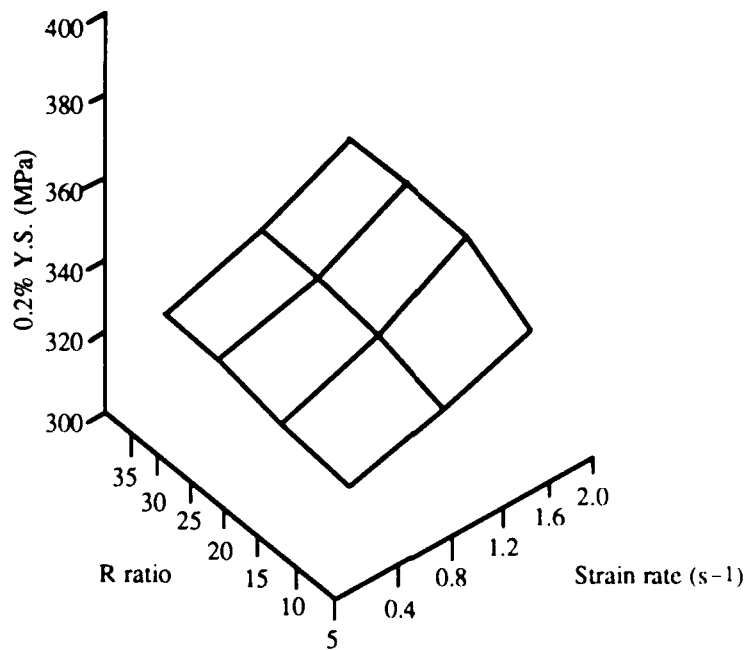
Extrusion parameters				Mechanical properties			
Temperature (°C)	R ratio	Aspect ratio	Strain rate (s ⁻¹)	0.2% Y.S. [MPa(ksi)]	U.T.S. [MPa(ksi)]	Elongation (%)	Fracture toughness [MPa√m (ksi√in.)]
500	16	4.3	0.57	307(44.5)	336(48.7)	2.1	12.2(11.1)
500	16	4.3	0.80	300(43.5)	324(47.0)	2.1	10.8(9.8)
500	16	4.3	1.66	295(42.8)	317(54.7)	4.4	—
450	16	4.3	0.57	301(43.7)	313(45.9)	2.6	10.7(9.7)
450	16	4.3	0.74	298(43.1)	319(46.3)	2.1	11.7(10.6)
450	16	4.3	1.71	295(42.6)	318(46.1)	3.5	10.8(9.8)
400	16	4.3	0.57	288(41.8)	317(46.0)	2.2	15.0(13.6)
400	16	4.3	0.91	291(42.2)	324(47.0)	2.7	14.3(13.0)
400	16	4.3	1.83	282(40.9)	322(46.7)	2.1	12.8(11.6)
350	16	4.3	0.57	297(43.1)	313(45.4)	1.9	11.6(10.5)
350	16	4.3	0.86	299(43.4)	314(45.5)	2.2	10.7(9.7)
350	16	4.3	1.60	300(43.5)	320(46.4)	2.8	14.1(12.8)
400	16	1.0	0.57	277(40.2)	316(45.8)	3.8	15.1(13.7)
400	16	1.0	0.86	279(40.5)	318(46.1)	4.0	12.8(11.6)
400	16	1.0	1.72	283(41.0)	321(46.6)	3.9	14.0(12.7)
400	31	5.0	0.55	270(39.2)	323(46.8)	4.5	14.5(13.2)
400	31	5.0	0.80	273(39.6)	325(47.1)	3.7	15.7(14.3)
400	31	5.0	1.94	275(39.9)	323(46.8)	2.9	13.4(12.2)
450	31	5.0	0.55	313(45.4)	336(48.7)	2.0	15.1(13.7)
450	31	5.0	1.73	316(45.8)	347(50.3)	2.6	14.1(12.8)
450	31	5.0	2.63	311(45.1)	351(50.9)	2.7	15.6(14.2)

87-224-188

Table 10. Effect of extrusion parameters on mechanical properties of Al-8Fe-7Ce in as-extruded condition.

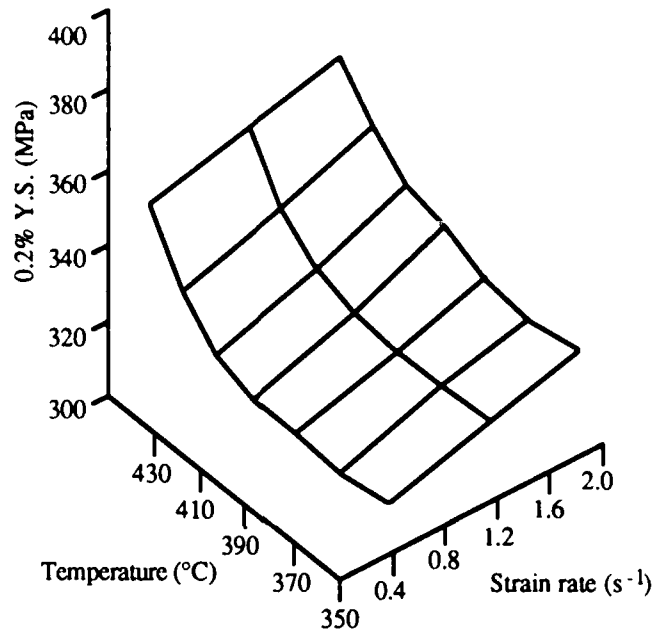
Extrusion parameters				Mechanical properties			
Temperature (°C)	R ratio	Aspect ratio	Strain rate (s ⁻¹)	0.2% Y.S. [MPa(ksi)]	U.T.S. [MPa(ksi)]	Elongation (%)	Fracture toughness [MPa√m (ksi√in.)]
425	6.6	2.7	0.44	328(47.6)	395(57.3)	13.1	21.0(19.1)
425	6.6	2.7	0.61	331(48.0)	391(56.7)	14.1	23.3(21.2)
400	6.6	2.7	0.44	338(49.0)	394(57.1)	14.6	23.2(21.1)
400	6.6	2.7	0.61	307(44.5)	384(55.7)	16.3	22.6(20.5)
375	6.6	2.7	0.44	353(51.2)	407(59.0)	12.4	22.3(20.3)
375	6.6	2.7	0.61	335(48.6)	399(57.9)	10.3	20.2(18.4)
375	6.6	2.7	1.09	347(50.3)	403(58.4)	10.9	22.9(20.8)
375	6.6	2.7	1.25	330(47.9)	394(57.1)	13.5	21.8(19.8)
350	6.6	2.7	0.40	358(51.9)	405(58.7)	10.6	23.3(21.2)
350	6.6	2.7	0.56	347(50.3)	398(57.5)	8.0	23.8(21.6)
375	6.6	1.0	0.40	345(50.0)	404(58.6)	10.1	21.3(19.4)
375	6.6	1.0	0.73	340(49.3)	394(57.1)	12.9	21.0(19.1)
375	9.9	4.0	0.38	354(51.3)	405(58.7)	12.3	19.8(18.0)
375	9.9	4.0	0.58	339(49.2)	391(56.7)	10.2	21.0(19.1)

87-224-186



87-224-179

Figure 51. Effect of extrusion R ratio and strain rate on room temperature yield stress of Al-3Li-1Cu-1Mg-0.2Zr isothermally extruded at 400°C.



87-224-178

Figure 52. Effect of extrusion temperature and strain rate on room-temperature yield stress of Al-3Li-1Cu-1Mg-0.2Zr isothermally extruded at a ratio of 16:1.

6. PUBLICATIONS AND PRESENTATIONS RESULTING FROM AFOSR SUPPORT

1. T. C. Peng, S. M. L. Sastry, J. E. O'Neal, and R. J. Lederich, Effects of Material Variables on Explosive Consolidation of Aluminum Alloys, American Society of Metals Meeting, Orlando, FL, October 1986.
2. S. M. L. Sastry, R. J. Lederich, and J. E. O'Neal, Influence of Metallurgical and Process Variables on the Consolidation, Densification, and Properties of Rapidly Solidified Aluminum Alloys, TMS-AIME Fall Meeting, Orlando, FL, October 1986.
3. S. M. L. Sastry, T. C. Peng, D. M. Bowden, and J. E. O'Neal, Microstructures and Mechanical Properties of Al-Li Alloys Produced by Conventional and Novel Consolidation Methods, 3rd International Aluminum-Lithium Conference, Oxford, England, July 1985.
4. T. C. Peng, S. M. L. Sastry, J. E. O'Neal, and R. J. Lederich, Explosive Consolidation of Aluminum Al-Li and Al-Fe-Ce Alloys, Explomet '85 International Conference on Metall. Applications of Shock-Wave and High-Strain-Rate Phenomena, Portland, OR, July-August 1985.
5. S. M. L. Sastry, R. J. Lederich, and J. E. O'Neal, Effects of Metallurgical and Process Variables on Aluminum Powder Consolidation, TMS-AIME Fall Meeting, Toronto, Canada, October 1985.
6. S. M. L. Sastry, T. C. Peng, and J. E. O'Neal, Novel Consolidation Methods for Rapidly Solidified Aluminum-Lithium Alloys, presented in the Symposium on Structural Aluminum Alloys for Aerospace Applications, TMS-AIME Fall Meeting, Detroit, MI, 16-20 September 1984.
7. S. M. L. Sastry, R. J. Lederich, and J. E. O'Neal, High-Temperature Flow Characteristics of Al-Li-Zr Alloys, TMS-AIME Annual Meeting, Los Angeles, CA, 26 February - 1 March, 1984.
8. Deformation Behavior of Rapidly Solidified Al-3Li Based Alloys, invited talk presented in the Department of Metallurgy and Materials Science, University of Toronto, Canada, 20 June 1984.
9. T. C. Peng, S. M. L. Sastry, and J. E. O'Neal, Explosive Compaction of Rapidly Solidified Aluminum-Alloy Powders, Met. Trans.

7. LIST OF PERSONNEL

The following MDRL personnel participated in this AFOSR-funded research:

S. M. L. Sastry - Principal Scientist

T. C. Peng - Scientist

J. E. O'Neal - Scientist

R. J. Lederich - Scientist

8. COUPLING ACTIVITIES WITH GROUPS DOING RELATED RESEARCH

1. Briefing on the objectives and approach of the program to AFWAL-ML personnel Dr. T. Ronald (LLS), Mr. W. Griffith (LLS), Lt. J. Adkins (LLS), and Dr. H. Gegel (LLM) at AFWAL-ML, Wright-Patterson Air Force Base, OH, 14 February 1984.
2. Briefing on the objectives, approach, and progress on MDRD/AFOSR Al-Li Alloy Powder Consolidation Research to Mr. Joe Collins (NASO) and Mr. A. P. Divecha (NSWC) on 14 August 1984.
3. Discussion with Prof. H. Fraser (University of Illinois, Urbana-Champaign) on Microstructures of Explosively Consolidated Al Alloy Powders, September 1983.

9. REFERENCES

1. S. M. L. Sastry, P. J. Meschter, J. E. O'Neil, and K. K. Sankaran, Microstructure and Properties of Powder Processed Aluminum-Lithium Alloys, AFOSR Contract No. F49620-79-C-0039, Final Report, MIT Report, May 1981.
2. R. E. Lewis, D. Webster, and I. G. Palmer, A Feasibility Study for Development of Structural Aluminum Alloys From Rapidly Solidified Powders for Aerospace Structural Applications, AFML-TR-78-111, July 1978.
3. W. M. Griffith, R. E. Sanders, Jr., and J. J. Hildeman, Elevated Temperature Aluminum Alloys for Aerospace Applications, in High-Strength Powder Metallurgy Aluminum Alloys, M. J. Kozak and J. J. Hildeman, eds. TMS-AIME, Warrendale, PA, 1982, p. 209.
4. J. P. Lyle, Jr., and W. S. Cebulak, Properties of High-Strength Aluminum P/M Products, Metals Eng. Quarterly 14 (1), 52 (1974).
5. A. P. Divecha and S. G. Fishman, Mechanical Properties of Silicon Carbide Reinforced Aluminum, New Matl. 3, 351 (1979).
6. S. L. Langenbeck, Elevated Temperature Aluminum Alloy Development, Interim Report, Air Force Contract F33615-81-C-5096, AFWAL MDDT, W-PARR, OH, December 1982.
7. R. W. Heckel, A New Approach to the Study of Powder Compaction, Progress in Powder Met. 17, 66 (1961).
8. D. Voss, Correlation of Processing Parameters, Microstructure, and Mechanical Properties of High Strength Powder Metallurgical Processed Aluminum Alloys, Ph.D. Thesis, DFVLR, Institut für Werkstoff-Forschung, Kolin, September 1979.
9. McDonnell Douglas Research Laboratories, Independent Research and Development Programs, 1983, MDC Q0866-4, 134001 and 1984, MDC Q0866-4, 144001.
10. V. D. Linse, ed., Dynamic Compaction of Metal and Ceramic Powders, National Academy of Sciences Report NMAB-394, Washington, DC, 1983.
11. O. V. Roman and V. G. Gorobtsov, Fundamentals of Explosive Compaction of Powders, in Shock Waves and High-Strain Rate Phenomena in Metals, M. A. Meyers and L. E. Murr, eds. (Plenum Press, 1981), p. 829.
12. Y. V. R. K. Prasad, H. L. Gegel, S. M. Doraivelu, J. S. Malas, J. F. Morgan, K. A. Lark, and D. R. Barker, Constitutive Behavior and Dynamic Modeling of Hot Deformation of a P/M 2024 Al Alloy with 20 Vol% SiC Dispersion, Air Force Materials Laboratory, Internal Report 1985.

END

8-87

DTIC